REPORT DOCUMENTATION PAGE		Form Approved OMB NO. 0704-0188

The public reporting burden for this collection of information is estimated to average 1 hour per response, including the time for reviewing instructions, searching existing data sources, gathering and maintaining the data needed, and completing and reviewing the collection of information. Send comments regarding this burden estimate or any other aspect of this collection of information, including suggesstions for reducing this burden, to Washington Headquarters Services, Directorate for Information Operations and Reports, 1215 Jefferson Davis Highway, Suite 1204, Arlington VA, 22202-4302. Respondents should be aware that notwithstanding any other provision of law, no person shall be subject to any oenalty for failing to comply with a collection of information if it does not display a currently valid OMB control number.
PLEASE DO NOT RETURN YOUR FORM TO THE ABOVE ADDRESS.

1. REPORT DATE (DD-MM-YYYY) 20-11-2014	2. REPORT TYPE Final Report	3. DATES COVERED (From - To) 17-Mar-2009 - 16-Feb-2014

4. TITLE AND SUBTITLE	5a. CONTRACT NUMBER
Final Report: Synthetic Aperture Acoustics (SAA) Detection of Camouflaged IEDs	W911NF-09-1-0082
	5b. GRANT NUMBER
	5c. PROGRAM ELEMENT NUMBER 633606

6. AUTHORS	5d. PROJECT NUMBER
Joseph Vignola, John Judge, Chelsea Good	
	5e. TASK NUMBER
	5f. WORK UNIT NUMBER

7. PERFORMING ORGANIZATION NAMES AND ADDRESSES	8. PERFORMING ORGANIZATION REPORT NUMBER
The Catholic University of America Office of Sponsored Programs 620 Michigan Ave, NE Washington, DC 20064 -0001	

9. SPONSORING/MONITORING AGENCY NAME(S) AND ADDRESS (ES)	10. SPONSOR/MONITOR'S ACRONYM(S) ARO
U.S. Army Research Office P.O. Box 12211 Research Triangle Park, NC 27709-2211	11. SPONSOR/MONITOR'S REPORT NUMBER(S) 55997-CS.8

12. DISTRIBUTION AVAILIBILITY STATEMENT

Approved for Public Release; Distribution Unlimited

13. SUPPLEMENTARY NOTES

The views, opinions and/or findings contained in this report are those of the author(s) and should not contrued as an official Department of the Army position, policy or decision, unless so designated by other documentation.

14. ABSTRACT

A synthetic aperture acoustic system was developed to detect roadside threats including IEDs and landmines. The technique uses audio-band sound broadcast from a compact trailer-mounted system to image the roadside perpendicular to the travel path. The area adjacent to the travel path is insonified and the microphone records the reflected acoustic signal. The travel of the transceiver creates a synthetic aperture that allows imaging of the scene. During the earlier phase of the project, a compact system was deployed, and experiments with pulse diversification was undertaken as well as a study of the effects of travel speed and path errors. Data was collected at Fort AP Hill

15. SUBJECT TERMS

Acoustic Imaging, Synthetic Aperture Acoustics, Acoustic Detection

16. SECURITY CLASSIFICATION OF:			17. LIMITATION OF ABSTRACT	15. NUMBER OF PAGES	19a. NAME OF RESPONSIBLE PERSON Joseph Vignola
a. REPORT UU	b. ABSTRACT UU	c. THIS PAGE UU	UU		19b. TELEPHONE NUMBER 202-319-6132

Standard Form 298 (Rev 8/98)
Prescribed by ANSI Std. Z39.18

Report Title

Final Report: Synthetic Aperture Acoustics (SAA) Detection of Camouflaged IEDs

ABSTRACT

A synthetic aperture acoustic system was developed to detect roadside threats including IEDs and landmines. The technique uses audio-band sound broadcast from a compact trailer-mounted system to image the roadside perpendicular to the travel path. The area adjacent to the travel path is insonified and the microphone records the reflected acoustic signal. The travel of the transceiver creates a synthetic aperture that allows imaging of the scene. During the earlier phase of the project, a compact system was deployed, and experiments with pulse diversification was undertaken as well as a study of the effects of travel speed and path errors. Data was collected at Fort AP Hill, and at the Night Vision Laboratory. The processed data were and further analyzed for characteristics and features amenable for discrimination. Additional design specification for a vehicle based SAA system was developed in conjunction Night Vision staff. Work related to measuring acoustic properties of both natural and anthropogenic materials relevant to outdoor imaging was executed. This work required the development of hardware such as vertical impedance tubes for both low (200-2000Hz) and mid frequency (500-8000Hz) ranges. The report presents and discusses results for several case studies of SAA imaging and acoustic material property characterization.

Enter List of papers submitted or published that acknowledge ARO support from the start of the project to the date of this printing. List the papers, including journal references, in the following categories:

(a) Papers published in peer-reviewed journals (N/A for none)

Received   Paper

TOTAL:

Number of Papers published in peer-reviewed journals:

(b) Papers published in non-peer-reviewed journals (N/A for none)

Received   Paper

TOTAL:

Number of Papers published in non peer-reviewed journals:

(c) Presentations

Non Peer-Reviewed Conference Proceeding publications (other than abstracts):

<u>Received</u>   <u>Paper</u>

TOTAL:

Peer-Reviewed Conference Proceeding publications (other than abstracts):

<u>Received</u>   <u>Paper</u>

01/18/2012   1.00   John Judge, Chelsea Good , Joseph Vignola, Steven Bishop, Peter Gugino, Mehrdad Soumekh. Synthetic
aperture acoustic imaging of canonical targets with a 2-15 kHz Linear FM chirp,
SPIE Defense Sensing . 25-APR-11, . : ,

08/31/2012   3.00   Aldo A. J. Glean, Chelsea E. Good, Joseph F. Vignola, John A. Judge, Teresa J. Ryan, Steven S. Bishop,
Peter M. Gugino, Mehrdad Soumekh. Synthetic aperture acoustic imaging of non-metallic cords,
SPIE Defence Sensing. 23-APR-12, . : ,

08/31/2012   4.00   John A. Judge, Joseph F. Vignola, Aldo A. J. Glean, Teresa J. Ryan, Chelsea E. Good, Peter M. Gugino,
Steven S. Bishop, Mehrdad Soumekh. DETECTION OF NON-METALLIC CORDS USING SYNTHETIC
APERTURE ACOUSTIC IMAGING,
ASME, 24th Conference on Mechanical Vibration and Noise (VIB) . 13-AUG-12, . : ,

TOTAL: **3**

Number of Peer-Reviewed Conference Proceeding publications (other than abstracts):

(d) Manuscripts

<u>Received</u>   <u>Paper</u>

01/18/2012 2.00 Joseph Vignola, John Judge, Chelsea Good , Steven Bishop, Peter Gugino, Mehrdad Soumekh.
SYNTHETIC APERTURE IMAGING OF SURFACE LAID TARGETS BY SOUND,
Sensing and Imaging: An International Journal (08 2011)

08/31/2012 5.00 Joseph F. Vignola, John A. Judge, Chelsea E. Good, Steven S. Bishop, Peter M. Gugino, Mehrdad
Soumekh. SYNTHETIC APERTURE IMAGING OF SURFACE LAID TARGETS BY SOUND,
Sensing and Imaging: An International Journal (10 2011)

    TOTAL: **2**

Number of Manuscripts:

Books

<u>Received</u>   <u>Book</u>

    TOTAL:

<u>Received</u>   <u>Book Chapter</u>

    TOTAL:

Patents Submitted

Patents Awarded

Awards

Graduate Students

NAME	PERCENT_SUPPORTED	Discipline
Aldo Glean	0.20	
Chelsea Good	1.00	
FTE Equivalent:	**1.20**	
Total Number:	**2**	

Names of Post Doctorates

NAME	PERCENT_SUPPORTED
FTE Equivalent:	
Total Number:	

Names of Faculty Supported

NAME	PERCENT_SUPPORTED	National Academy Member
Joseph Vignola	0.08	
John Judge	0.08	
FTE Equivalent:	**0.16**	
Total Number:	**2**	

Names of Under Graduate students supported

NAME	PERCENT_SUPPORTED	Discipline
Chelsea Good	0.25	Mechanical Engineering
Nicole Bull	0.05	Mechanical Engineering
FTE Equivalent:	**0.30**	
Total Number:	**2**	

Student Metrics
This section only applies to graduating undergraduates supported by this agreement in this reporting period

The number of undergraduates funded by this agreement who graduated during this period: 2.00

The number of undergraduates funded by this agreement who graduated during this period with a degree in science, mathematics, engineering, or technology fields:...... 2.00

The number of undergraduates funded by your agreement who graduated during this period and will continue to pursue a graduate or Ph.D. degree in science, mathematics, engineering, or technology fields:...... 2.00

Number of graduating undergraduates who achieved a 3.5 GPA to 4.0 (4.0 max scale):...... 1.00

Number of graduating undergraduates funded by a DoD funded Center of Excellence grant for Education, Research and Engineering:...... 0.00

The number of undergraduates funded by your agreement who graduated during this period and intend to work for the Department of Defense 2.00

The number of undergraduates funded by your agreement who graduated during this period and will receive scholarships or fellowships for further studies in science, mathematics, engineering or technology fields:...... 1.00

Names of Personnel receiving masters degrees

NAME
Chelsea Good
Total Number: 1

Names of personnel receiving PHDs

NAME
Aldo Glean
Total Number: 1

Names of other research staff

NAME	PERCENT_SUPPORTED
FTE Equivalent:	
Total Number:	

Sub Contractors (DD882)

Inventions (DD882)

Scientific Progress

The project resulted in the development of a working synthetic aperture acoustics system for road side imaging. The system was used in a verity for data collections on a host of targets and situations. This data can be used to validate productive models and a database of automatic target recognition (ATR) algorithm training. The project also resulted in the development of apparatus and instrumentation for characterizing the acoustic properties of soils with and without plant matter under differing conditions. This information is also necessary for modeling outdoor acoustic imaging.

Technology Transfer

The SAA technology was transferred to the Army Night Vision Labratory. Specifically Dr. Steven Bishop, of US Army RDECOM CERDEC NVESD, RDER-NVC-GA, 10221 Burbeck Rd. Ft. Belvoir, VA 22060. Tel: (703) 704-1037

Synthetic Aperture Acoustic Imaging for Roadside Detection of Solid Objects

Final Report for The US Army Research Office Terrestrial Sciences ATTN: AMSRL-RO-RI P.O. Box 12211 Research Triangle Park, NC 27709-2211

Joseph Vignola, John Judge and Chelsea Good

Abstract

A synthetic aperture acoustic system was developed to detect roadside threats including IEDs and landmines. The technique uses audio-band sound broadcast from a compact trailer-mounted system to image the roadside perpendicular to the travel path. The area adjacent to the travel path is insonified and the microphone records the reflected acoustic signal. The travel of the transceiver creates a synthetic aperture that allows imaging of the scene. During the earlier phase of the project, a compact system was deployed, and experiments with pulse diversification was undertaken as well as a study of the effects of travel speed and path errors. Data was collected at Fort AP Hill, and at the Night Vision Laboratory. The processed data were and further analyzed for characteristics and features amenable for discrimination. Additional design specification for a vehicle based SAA system was developed in conjunction Night Vision staff. Work related to measuring acoustic properties of both natural and anthropogenic materials relevant to outdoor imaging was executed. This work required the development of hardware such as vertical impedance tubes for both low (200-2000Hz) and mid frequency (500-8000Hz) ranges. The report presents and discusses results for several case studies of SAA imaging and acoustic material property characterization.

Contents

Chapter 1

Introduction

Drs. Vignola and Judge, along with a group of student research assistants in the Mechanical Engineering Department at the Catholic University of America, have continued a multi-year effort to determine the feasibility of using synthetic aperture acoustic (SAA) imaging to detect camouflaged IEDs. This report describes the progress made over the past year. CUA has worked with Dr. Mehrdad Soumekh of the electrical engineering department at SUNY Buffalo was well as Dr. Steven Bishop and Peter Gugino of the US Army Night Vision Laboratory and Dr. Lesile Collins' group at Duke University.

Synthetic aperture acoustics (SAA) is a technique used for forming images of objects based on the reflection of sound waves. This technique is similar to side scanning sonar and synthetic aperture radar in that an image is formed from backscatter collected by a receiver that traverses a path along the side of a target field. The synthetic aperture approach uses repeated excitation signals that originate from different the spatial locations and takes advantage of coherent reorganization of data from each excitation signal to produce images of higher resolution that can be produced by conventional acoustic array imaging. This document describes two SAA systems used in a laboratory setting and in the field that can be deployed to quantitatively inspect wall structures with the objective of potentially detecting anomalous configurations, i.e., degraded CMU, delaminated stucco surfaces, and inclusions or occlusions within walls. Initial published work on airborne SAA was first published by Soumekh[1] and a down-looking SAA system using multiple receivers and a single transmitter was investigated by Frazier[2]. A great deal of the literature and specific processing techniques from both synthetic aperture sonar (SAS) and synthetic aperture radar (SAR)[3, 4] are directly applicable to SAA. The work presented here followed the nomenclatures for synthetic aperture systems and give by Gough's and Hawkins'[5] for synthetic aperture sonar (SAS). In this application, SAA serves as a noninvasive inspection technique with a standoff distance that provides a measure of safety for personnel and equipment.

1.1   Scope of this Document

During the initial period of this project, CUA used a mobile scanning stage carrying an acoustic transceiver system to collect data on a variety of surface-laid targets in a variety of situations. Development of that prototype system, and results of data collection using it has been described in previous annual reports. Those data collections occurred both indoors and outdoors at CUA and on several occasions Ft. AP Hill in Virginia. In addition to demonstrating some of the capabilities of the system and supporting the validity

of the SAA approach, the data acquired in these tests informed the development of a second-generation mobile system for SAA data collection, which was assembled and tested during spring and summer 2011. This system mounts the microphone, loudspeaker, and ancillary equipment on a trailer that can be towed behind any ordinary vehicle. A detailed description of the second-generation, trailer-based system was provided in the 2011 progress reported (a condensed summary of the system design is provided below). In the later period, 2012-13, CUA used a trailer based system to collect roadside data. These systems will be described in some detail along with representative dated form each. In addition to the SAA systems, two impedance tubes where constructed for characterizing soil samples where designed, fabricated and used for parameter estimation in models.

Chapter 2

Laboratory SAA System

During the project CUA built two SAA systems the first was a laboratory based system 5 meters in length and the second was a trailer based system for field collections. This trailer based system will be described in the next chapter.

The first generation system was built for laboratory measurements on a 5m scanning rail. The system was used in both indoor and outdoor environments but was somewhat cumbersome. The system is should in Figs. 2.1 and 2.2.
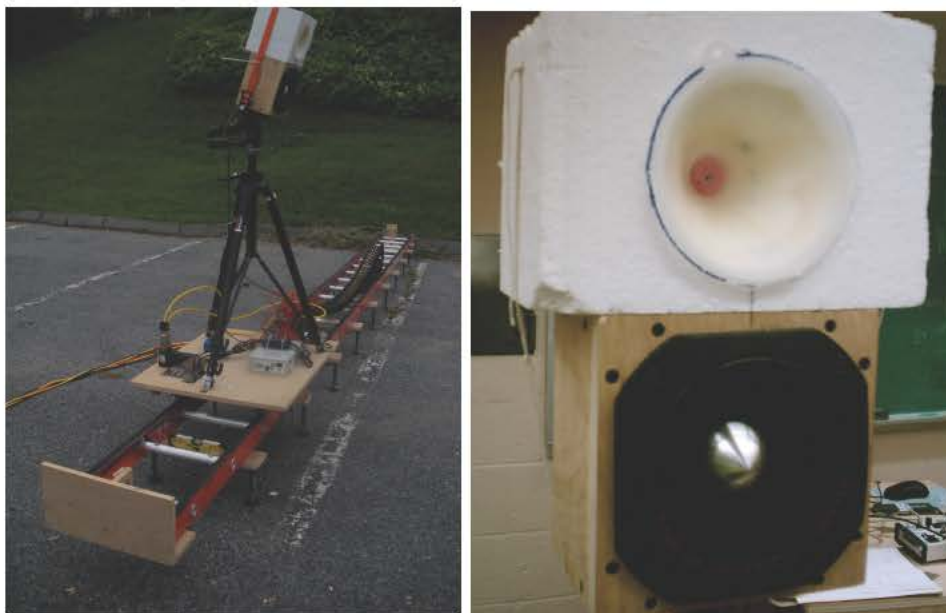

Figure 2.1: (left) The rail based system consists of a tripod mounted transceiver that traverse a straight rail. (right) Close up of the acoustic transceiver.

This system was used to demonstrate that an acoustic imaging system could distances similar shaped objects composed of different materials. An example is the student on construction blocks. One was an actual construction cinder block, the second was a block of foam covered we a thin (approximately 1/4")

Figure 2.2: (left) The control station for the rail based system consists of a PC with a National Instruments data acquisitions system, audio filters and power amplifier and all other support electronics. (right) 5m rail mounted monostatic imaging system transmits and receives acoustic chirps (2-15kHz) to and from a collection of surface laid targets.

masonry skin and the final was similar masonry covered block with a concealed dense metal object. See Fig. 2.3.

2.1 Data Collection Procedure

This system is used for both indoor and outdoor measurements. For the indoor test range, targets are suspended in the center center of a test range which consists of an open room with a pit (see Fig. 2.1) measuring approximately 4 meters square and 3 meters deep. Target are positioned vertically at the level of the transceiver. See Fig. 2.1. This system was also used for image generation with surface laid objects. See 2.2. Here an array of targets are positioned on the ground 2-10 m from the scanning rail. As the scanner traverses its linear path, the target is exposed to the 10 ms acoustic linear FM chirp with frequency content ranging from 6 to 14 kHz at approximately $100dBre20\mu Pa$. The transceiver moves incremented at 1 cm intervals over the 5 m track or flight path. This resulted in 500 synthetic aperture data points.

2.2 Results for the Block Testing

The first test targets SAA imaging system shown as wavefront reconstructions [6] are shown in Figs. 2.2 to 2.4. Each target was positioned in the center of the indoor range on a suspension carriage design to have a minimum scattering cross-section. The collected acoustic backscatter produces images of the full scene which includes much more that the target of interest. An example can be seen in Fig. 2.1. These

Cinderblock   Foam block   Weighted foam block

Isometric and translucent view
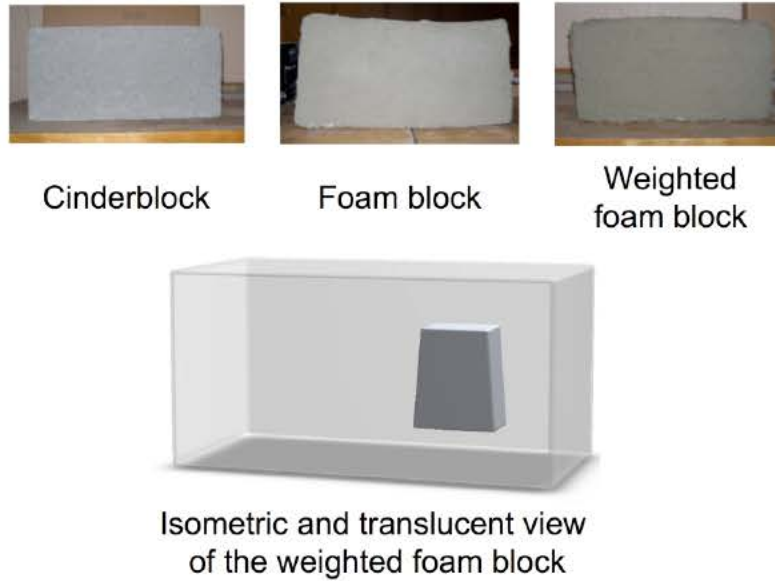of the weighted foam block

Figure 2.3: Illustration of the three block targets used in validating the SAA approach.

Figure 2.1: The lab SAA range is shown with a suspended 10 cm diameter steel sphere.

are reflections from the finned housing in the fluorescent lighting. The back counter, desks and wall of the laboratory are at about 6 m to 8 m slant range.

Figures 2.2 to 2.4 are the reconstructions of the interrogated scene with the funnel apparatus described above. Three different targets were positioned at the slant range of 2.4 m for these experiments: layered foam block (LFB, Fig. 2.2); weighted block (WB, Fig. 2.3); and concrete block (CB, Fig. 2.4). Conventional methods for identifying targets in a radar or acoustic imaging system (also known as Automatic Target Recognition, ATR) approach this issue as a pattern recognition problem in which the user attempts to classify targets based on their image features. This view of ATR originally comes from target recognition problems in visible imagery (e.g., images from a camera). However, SAR or SAA images of the targets
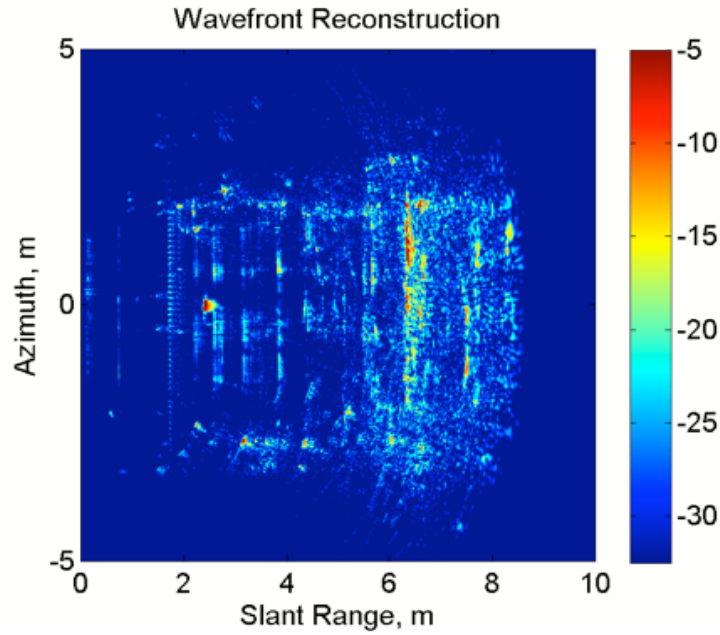
Figure 2.1: An illustration of acoustic wavefront reconstruction of a 0.2 m square aluminum plate located at approximately 2.2 meter slant range and 0 degrees azimuth.
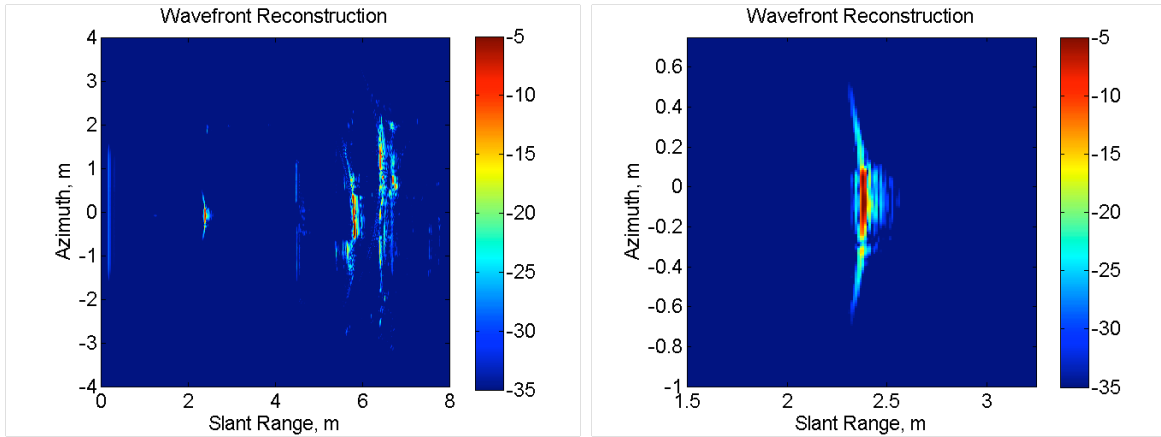

Figure 2.2: (left) Wavefront Reconstruction of a construction cinder block suspended and other scattered in the lab test range. (right) Digital spotlight that isolates the cinder block.

of interest within the radiated band appear as blobs[6]; that is, there are no distinct features in their SAR/SAA images for conventional pattern-based ATR. We have developed alternative ATR algorithms for SAR that are based on reconstructing the complex (phase as well as magnitude) SAR/SAA signature of these targets in the original measurement domain, that is, the frequency and aspect angle domains[7]. This approach that we refer to as inverse imaging, has the potential to reveal more distinct features for ATR purposes.

As mentioned earlier, the objective in inverse imaging is to reconstruct SAR/SAA signature of a target
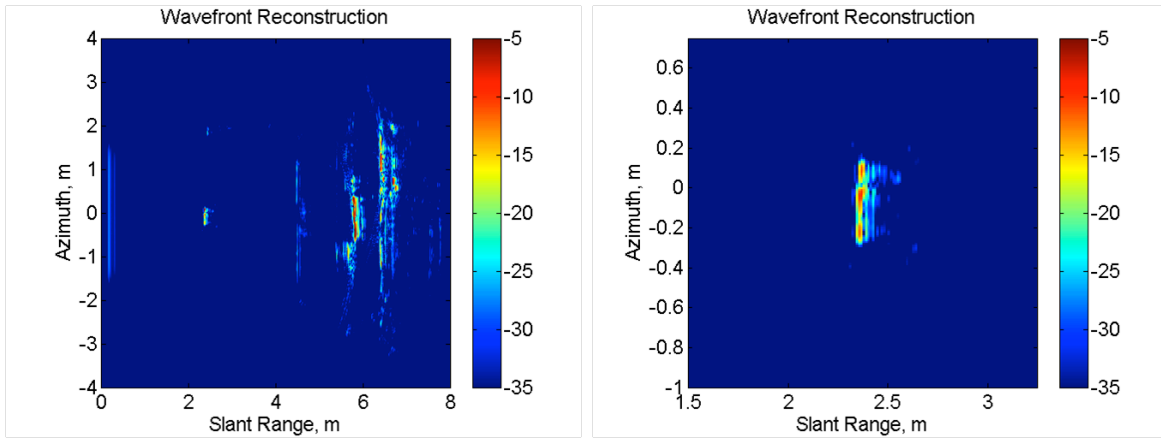
Figure 2.3: (left) Wavefront Reconstruction of a construction foam block suspended and other scattered in the lab test range. (right) Digital spotlight that isolates the foam block.
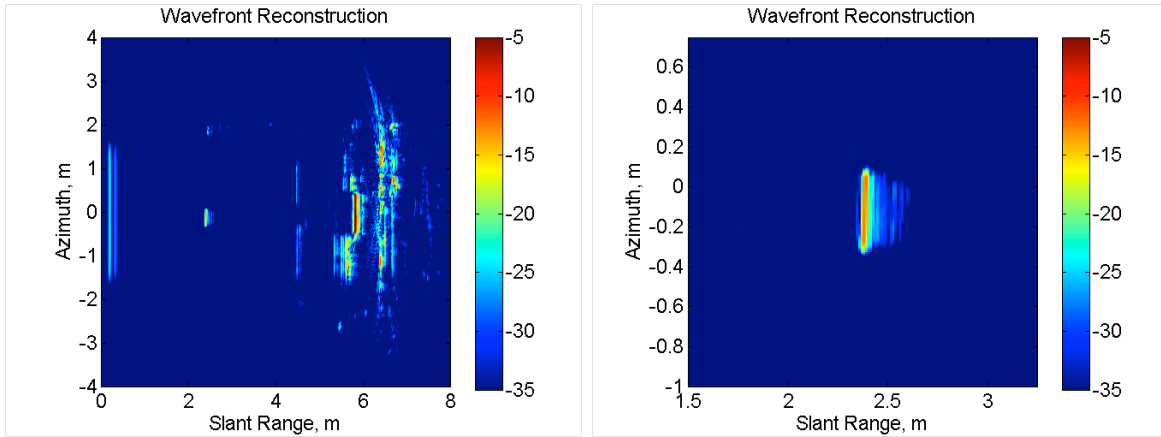

Figure 2.4: (left) Wavefront Reconstruction of a construction foam block with an embedded scatterer suspended and other scattered in the lab test range. (right) Digital spotlight that isolates the target block.

from its formed SAR/SAA image. In a SAR/SAA image, individual targets appear localized (focused) around a region (i.e., a blob); this is not the case in the original measurement domain with hyperbolic SAR/SAA signatures. One can extract each 'suspected' blob image (a process called digital spotlighting), and then perform the inverse of the signal processing algorithm that converted the original measured data into the SAR/SAA image to reconstruct the hyperbolic SAR/SAA signature of the suspected blob. Figure 2.5 shows a block diagram for digital spotlighting and inverse imaging. Figure 2.6 shows the magnitude and phase signatures of the three targets in the reconstructions of Figures 2.2 thorugh 2.4 using the inverse imaging. Note that the three targets exhibit distinct attributes or characteristics in the measurement frequency and aspect angle domains. The Acoustic Magnitude Signature plots have the units of dB. Acoustic magnitude is the real part of the sound pressure comprising the synthetic aperture and frequency spectrum. Figure 2.6 is a composite of the three respective targets, their acoustic magnitudes and acoustic phase response in the acoustic spectral range from 6 kHz to 14 kHz.
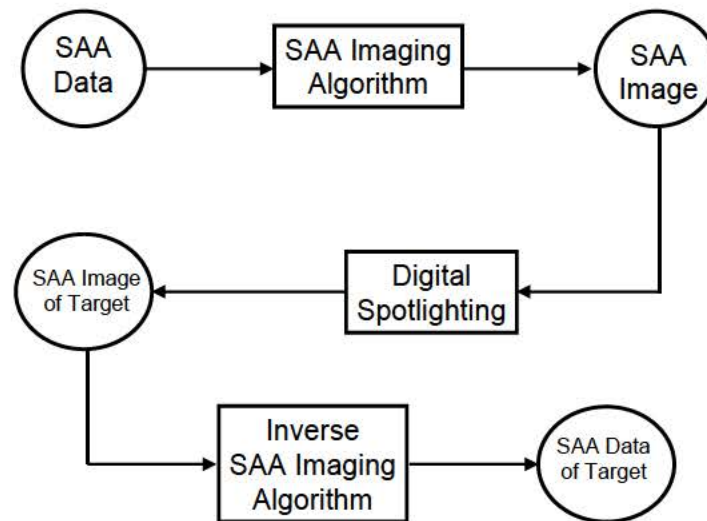
Figure 2.5: Block Diagram of Target Signature Reconstruction via Digital Spotlighting and Inverse Imaging.

The layered foam block magnitude signature exhibits a fairly uniform distribution over the radiated angular interval of $-25°$ to $25°$. That is dictated by the funnel spatial filter. On the other hand, the cinder block shows a strong magnitude signature over a small angular interval; this is referred to as 'flash' signature that is typical of hard-scattering flat surfaces. The weighted block also shows a wide-angle signature; however, the distribution shows nonuniformity. The phase signatures also show distinct features. These features and nonuniformities in both the magnitude and phase signatures are potentially exploitable characteristics to be investigated for object discrimination. We are in process of analyzing these distributions to acquire a better understanding of them.

One of the methods to analyze the magnitude and phase signatures is to develop parametric models for them at each radiated frequency. But examination of the two dimensional acoustic phase plots one can make qualitative measures. Here one can easily see the layered foam block has a uniform phase about zero degrees azimuth then a steep phase gradient occurs as the absolute azimuth angle increases. The appearance is very symmetric about zero degrees azimuth. In the case of the cinder block the uniform phase region about zero degrees azimuth is comparatively narrower and then as the absolute azimuth angle increases the phase variation becomes more pronounced and wider after which the steep phase gradient then occurs. The appearance is somewhat symmetric about $0°$ azimuth. The last example is the weighted foam block that has even wider uniform phase regions than the priors and they have phase discontinuities over frequency comparable frequencies and have even larger phase magnitudes. The appearance is not very symmetric about zero degrees azimuth.

These are only one example that validated the approach. The next step was to develop a system that could be used to collect data along a roadside from a vehicle.
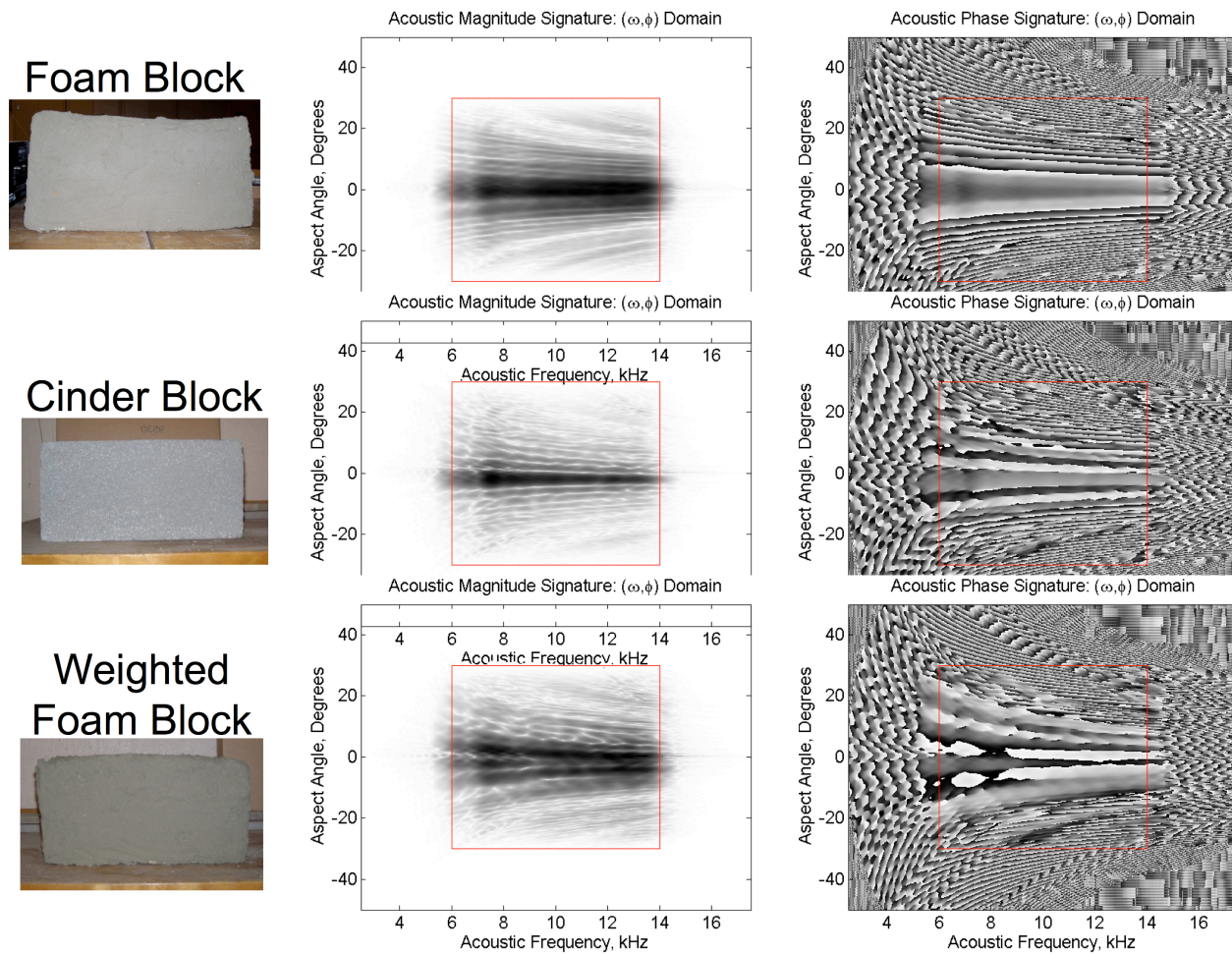
Figure 2.6: SAA images of the target structures where created to shown that the internal structure could be revealed.

Chapter 3

Field SAA System

The concept for the field SAA system was to re-implement the lab system on a trailer that would be pulled behind a vehicle for scanning long sights. Initially the goal was to have a self powered, laptop controlled system that could be pulled by any vehicle and was capable of scanning 100 meters at a time. The operator would set in the passenger set of the vehicle with the laptop while the drive would cruse along a path.

The field system evolved from laboratory system and the first generation implementation, shown in Fig. 3.1 simply used the control station from that system but mounting it directly on a trailer. The block diagram of the field SAA system is shown in Fig. 3.2.

3.1 System Refinements

A number of system capabilities related to both software and hardware were made to the trailer-based system and a design for a vehicle based system was developed. The software refinements included:

1. Curved path capably for the trailer-based system requires precise knowledge of the travel path of the transceiver for image formation.

2. Pulse diversification with allows the excitation signal duty cycle to be effectively 100%.

3. Development of real-time diagnostics for system software.

The hardware refinements included:

1. Addition of a digital compass for orientation compensation.

2. Alternative AC system power

The objective of these refinements was to in the rate of advancement of the system, improve image quality by increasing the signal to noise ratio and reducing or eliminating spatial aliasing. The second work task executed during this period of performance is related to the characterization for the acoustic properties of natural acoustic scatterers and absorbers found in the environments of the images. In addition, an acoustic impedance tube was constructed for measuring the acoustic properties of materials including

Figure 3.1: The first generation of the SAA field system used a desktop computer as non-specialized laboratory instrumentation.

soils, gravel, and grass. This task is not directly related to the prototype SAA hardware, but necessary to make further progress on demonstrating the feasibility of the SAA concept, and is also described in detail in this report along with results from soil samples.

3.1.1 The SAA System Hardware

Figure 1 shows a schematic of the trailer-based system in use for this work. The system is now outfitted with digital wheel encoders and an Ocean Server digital compass that provides travel orientation and tilt data to the data records via USB connection acquisition computer. This compact device (≈ 1 gram) has 0.5 degree resolution. The system power for the data acquisition and power amplifier had proven problematic because of noise. Several alternatives were considered including a gasoline power Honda generator and a DC to AC power inverter. In the end a hybrid approach was implemented was implemented.
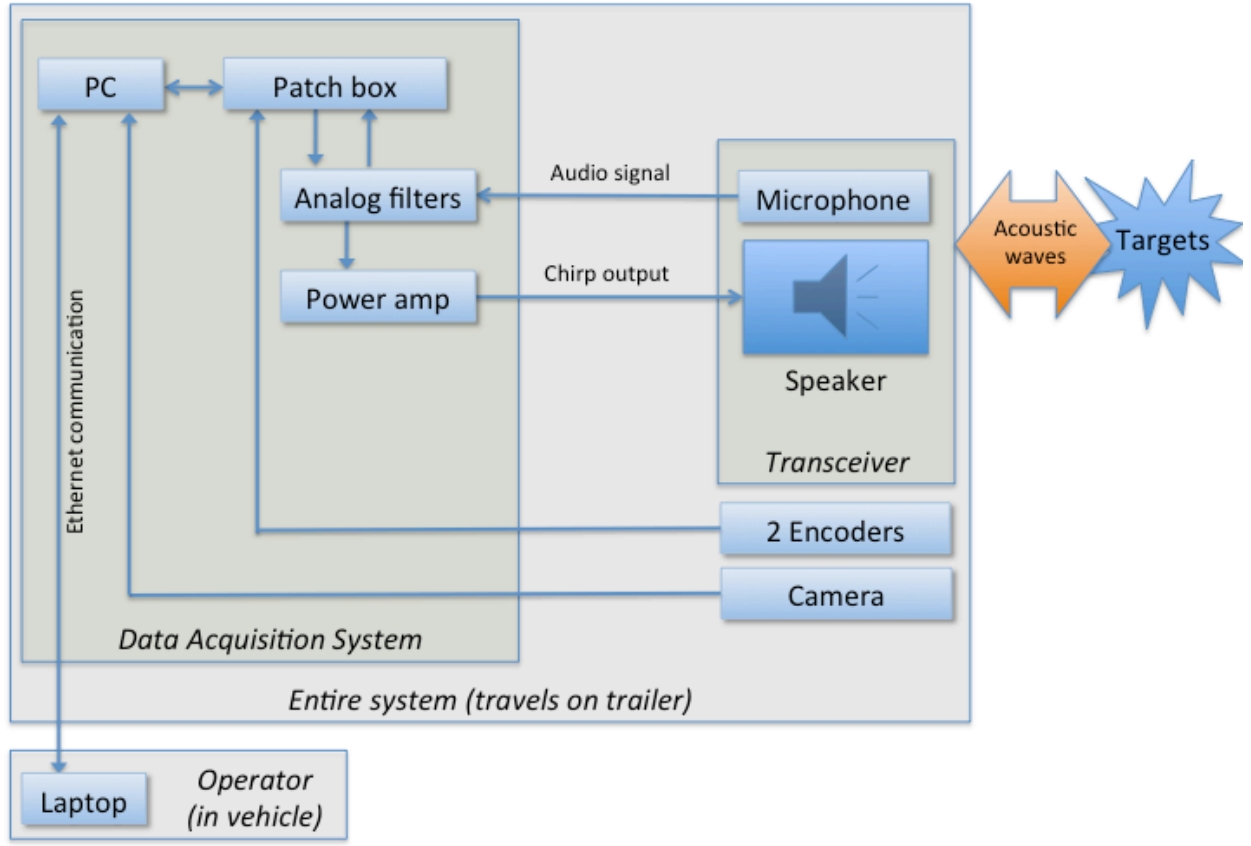
Figure 3.2: Initial block diagram of the trailer-based synthetic aperture system.

3.1.2 Path Correction

Unlike the earlier rail-based system used in the initial years of this project, the trailer-based system is not limited to a straight path. A significant effort has been applied during this year to develop an appropriate path-correction procedure that accounts for the potentially curved path of the transceiver. An initial path correction algorithm was developed earlier in the program and implemented into the SAA imaging code, based on the use of two rotary encoders mounted near the two wheels of the trailer. These two encoders are sampled evenly in time and each produce a sequence of positions once the tire circumference and gear ratio for the encoder wheel are considered. The geometry of the path of the trailer is shown in Figs. 3.1 and 3.2. In Fig. 3.2, the z-axis is the nominal travel axis and the r-axis is the nominal direction of propagation of the outgoing sound. The block diagram of the field SAA system is shown in Fig. 3.2 The distance each wheel center travels in during a sample interval is related travel geometry by.

$$ds_1(n) = \Delta\theta(n)\left(R(n) + \frac{L}{2}\right) \tag{3.1}$$

$$ds_2(n) = \Delta\theta(n)\left(R(n) - \frac{L}{2}\right) \tag{3.2}$$

Figure 3.1: Trailer layout and dimensions are shown.

Where $\Delta\theta(n)$ is the change in the trajectory angle and $R(n)$ is the radius of curvature in the n'th time interval. If we subtract these two

$$ds_2(n) - ds_1(n) = L\Delta\theta(n) \tag{3.3}$$

Or

$$\Delta\theta(n) = \frac{ds_2(n) - ds_1(n)}{L} \tag{3.4}$$

This change of angular orientation is now compared to the change in orientation measured by the digital compass. When the error exceeds a threshold, about 2 degrees, the initial angle is reset. The ratio of the
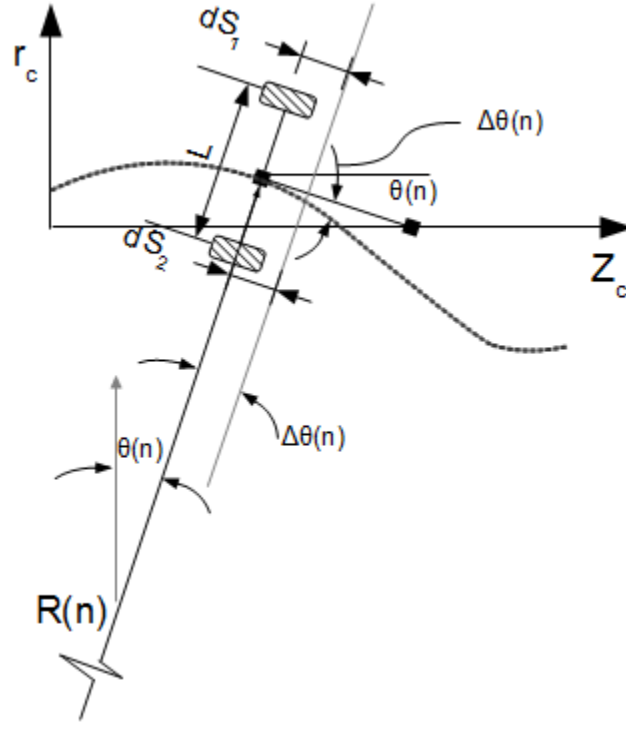
Figure 3.2: The geometry of the trailer path is shown.

travels vectors is related $R(n)$ by

$$R(n) = \frac{L}{2}\left(\frac{ds_1(n) + ds_2(n)}{ds_1(n) - ds_2(n)}\right) \tag{3.5}$$

A further simplification can be made by defining an average distance traveled, $d\bar{s}$ and a travel difference, Δds as

$$d\bar{s}(n) = \frac{ds_1(n) - ds_2(n)}{2} \tag{3.6}$$

$$\Delta d\bar{s}(n) = ds_1(n) - ds_2(n) \tag{3.7}$$

Given this we can solve for the travel vector as

$$\Delta x_c(n) = d\bar{s}(n)\cos(\theta(n)) \tag{3.8}$$

$$\Delta y_c(n) = d\bar{s}(n)\sin(\theta(n)) \tag{3.9}$$

This travel path is then determined by defining the initial coordinates as $x_c(1) = 0$ and $y_c(1) = 0$ and using

$$\Delta x_c(n+1) = x_c(n) + \Delta x_c(n) \tag{3.10}$$

$$\Delta y_c(n+1) = y_c(n) + \Delta y_c(n) \tag{3.11}$$

The digital compass was added to the system to provide orientation information $\theta(n)$. The test used to validate this approach is to image a nominally straight target (roadside curb) and compare that result

to that generated by the encoders and compass. Figure 3.3 shows this comparison. (A separate test was conducted that showed the target surface was straight to within 4cm over the 60m.). This plot indicates that the travel path determined from encoders and digital compass is within 10cm of the travel path determined by the acoustic echo and, most importantly, that the errors do not accumulate.
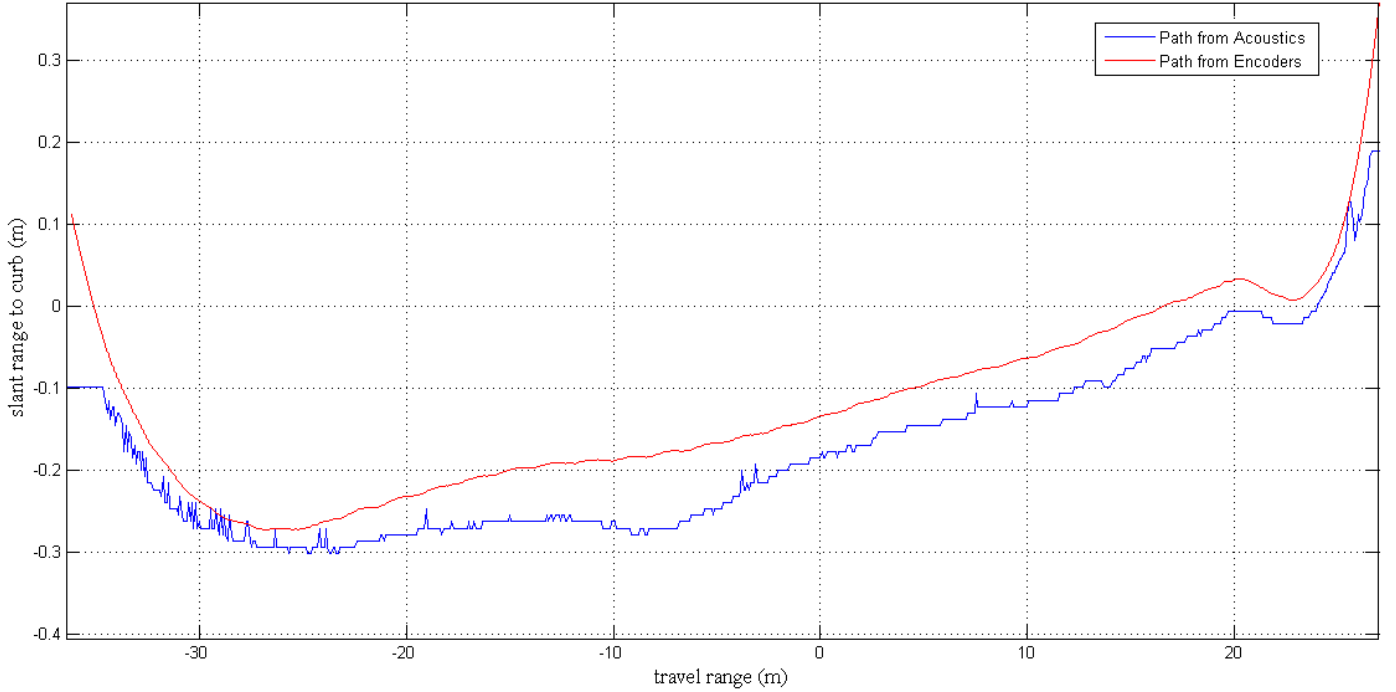

Figure 3.3: Path measurements based on acoustic data (blue) and encoder data (red).

Pulse Diversification and Image Resolution

Image resolution is limited by spatial repetition rate, ξ which is the number of acoustic excitation signal broadcast per distance traveled. The spatial repetition rate is related to the temporal repetition rate, ϕ and travel speed, v_t by $\xi = \phi/v_i$. This implies that to increase the spatial repetition rate one would need to increase the temporal repetition rate or reduce the travel speed, which is much less desirable. If the same excitation signal is broadcast repetitively (homogenous excitation) then the slant range, R_{slant} is related to the repetition interval (the reciprocal of the repetition rate, f_{rep}) by.

$$R_{slant} = \frac{c}{2f_{rep}} \tag{3.12}$$

This expression assumes that any targets beyond this slant range do not have target strength big enough to produce a significant scattering contribution. This is often not a reasonable assumption.

An alternative to homogenous excitation is pulse diversification where diverse collection of signals with common bandwidth are used in succession. A collection of matched filters, one for each excitation signal, are then used to associate the different return signal with the appropriate source signal. For this work five

linear FM chirps with a band with of 2-17 kHz and durations of 15, 20, 25, 30, and 35 ms along with five additional chirps that are simply the time revered versions of the first group are also include yielding ten distinct excitation signals. These ten excitation signals are then shifted in time and summed so that one of the signals begins every 5 ms. This signal can then be repeated every 50 ms.

Real-Time Data Visualization

New software for utilities for real-time data visualization of images was implemented. An example is show in Fig. 3.4. These images show no-metallic cords placed on the ground.
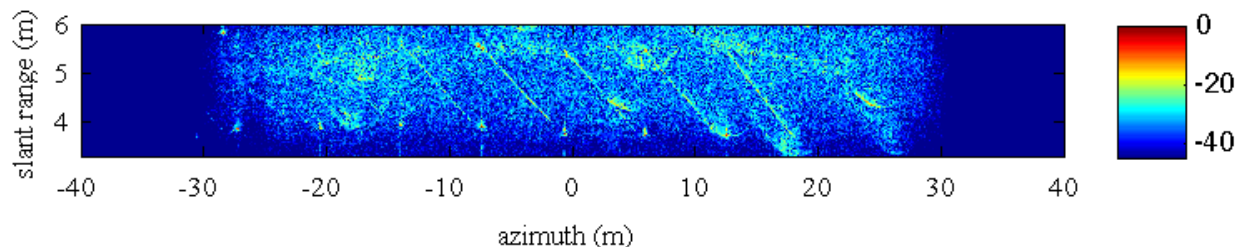

Figure 3.4: Acoustic images of road-side non-metallic cords.

Chapter 4

Field Measurements

The system was used for many studies. Here we present a case study of surface laid nylon cord as well as several other surface laid targets.

4.1   Nylon Cord Study

The SAA system was used to study the detectability of non-metallic cords laid on the ground surface. Detection of non-metallic targets via acoustics is of interest because of the low radar scattering cross-section of such objects. Experiments were conducted along a roadside on the campus at the Catholic University of America, with significant levels of typical ambient urban noise, including pedestrian, wind, automobile, rail, and air traffic, and wind background noise.

4.1.1   Targets

Six braided nylon cords with diameters 3.2, 4.8, 6.4, 9.5 12.9 and 15.9mm (1/8, 3/16, 1/4, 3/8, 1/2, and 5/8 inch) were laid at three angles (10°, 20°, and 30° from parallel) along a sidewalk running parallel to the roadway. The targets are shown in Fig. 4.2 The imaged scenes also include paved and grass-covered ground surfaces, curbs, road signs, small trees, and metal retroreflectors added to the image as fiducials.

For each data collection, the SAA system trailer was towed behind a pickup truck at speeds between 1 and 2 mph. (Future improvements to the system, including broadcasting of diverse pulses at a faster repetition rate, will allow for increased vehicle speed.) There is essentially no limit to the duration for which data can be collected (other than that imposed by the finite storage space for data on the PCÕs drive), and for the results presented here, that the total distance traveled is typically over 100 m. The resolution of the image is therefore not limited by the aperture created by the sensor motion, but by the directionality of the speaker and microphone and the decrease in sound pressure level due to spherical spreading with range, i.e., the acoustic scattering from a given location in the image is only significant at a certain range of microphone locations, not over the entire 100 m+ travel distance.

The reconstructed image from a typical data collection is shown in Fig. 4.1. In this case, the image incorporates a 100 m distance along the roadside (azimuth) and 10 m perpendicular to the road (range from 1 to 11 m). The same data is presented twice, once with azimuth and range axes scaled equally (top of Fig.
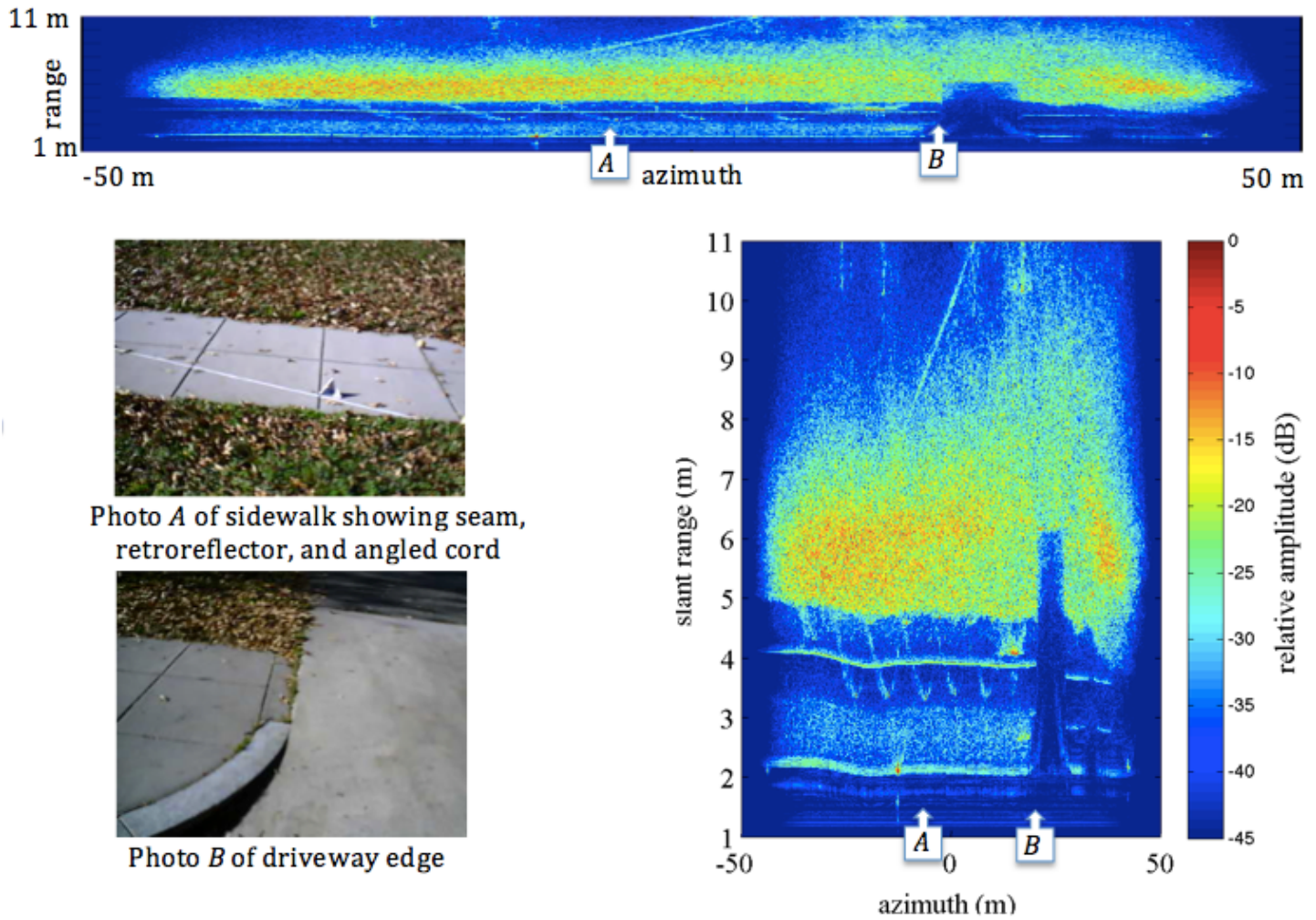
Figure 4.1: Typical Data collected with the SAA system. The transceiver traversed a 100m section of road for this collection that included surface laid object on sidewalk. The targets included retroreflectors places for calibration and nylon cords of various diameters laid at a 20° angle relative to the sidewalk. (top) Shows the data scaled equally in the azimuth and range directions. (right) Shows the same data with the range dimension exaggerated to illustrate the target features. The two photos (middle and lower left) show the targets. The A an d B labels indicate the corresponding locations of these photos in the top and right images.

4.1) and the other with range scale greatly exaggerated (right of Fig. 4.1). The nearly straight line near the bottom of each image (range 2 m) is the curb separating the road from a grassy area approximately 1 m wide, which is broken by a driveway perpendicular to the road (near +25 m azimuth, and shown in photograph B). A sidewalk approximately 1.5 m wide shows significantly lower acoustic scattering than the grass-covered region between sidewalk and curb, or than the grass-covered hill beyond the sidewalk. However, there is a strong acoustic return from a seam in the sidewalk concrete that runs down the center of the sidewalk (there are also seams perpendicular to the roadway at regular intervals, but these do not generate significant acoustic return). Note that the horizontal lines in the image resulting from the curb

and sidewalk seam are not perfectly straight Ð the deviation is due primarily to small deviations in the path of the vehicle and trailer along the road.

4.1.2 Acoustic Visibility of Nylon Cords

In the images in Fig. 4.1, the nylon cords are clearly visible laid along the sidewalk at a 20° angle relative to the roadway. In this particular case, cords of all diameters are visible, with stronger return evident from the larger diameter cords (towards the left in the images). Note that the largest diameter cord (at far left) is a shorter length, and does not extend completely across the sidewalk.

The affect of changing the angle of the cords relative to the sidewalk (which is nominally parallel to the transceiver path) is shown in right side of Fig. 4.1. These images show the portion of each data set containing the nylon cords (approximately 3 to 5 m in range and -40 to +20 m azimuth using the coordinates from Fig. 4.1). Again, cords increase in diameter from right to left. At a 10° angle, all six cords are clearly visible, with signal-to-noise ratio exceeding 20 dB for the largest cords. The decrease in acoustic return with increasing angle is significant, such that the cords are barely visible in the 30° case. Note that the scene includes a single metal retroreflector at the beginning (bottom right end) of each rope, and these are still clearly visible in the 30° case, while the cords themselves are only barely visible against the background return from the sidewalk.

In the images on right side of Fig. 4.1, the frequency content for one image (in this case, for cords laid at 20°) is separated in three octave bands (2-4 kHz, 4-8 kHz, and 8-16 kHz). The results show that the low frequency return contains little to no information about the location of the cords, and the targets become more visible as the acoustic wavelength approaches the cord diameter.

4.1.3 Conclusion for Cord Study

The goal of this work is to demonstrate the detectability of a range of cord diameters and explore other experimental parameters that affect this detectability. These parameters include cord angle relative to the transceiver path, ambient noise, and acoustic excitation characteristics such as chirp frequency, duration, source level, and directionality of the speaker and microphone. The preliminary results presented in this paper demonstrate that non-metallic cords can be detected acoustically when the angle to the transceiver path is sufficiently small and the acoustic wavelengths approach the cord diameter.

The SAA approach provides a means of centimeter scale detection of nonmetallic items. The equipment required for this type of acoustic measurement is significantly less costly than radar. Additionally, the acoustic approach can be used in conjunction with radar to produce a richer set of information than either approach alone. This technology allows for discrimination of a set of targets that has some overlap with the set detectable by radar with an important addition. Dielectric materials such as the nylon cord studied here are invisible to radar but clearly detectable by SAA. The target clutter with this technology arises from a different combination of geometric and physical properties than does clutter in radar measurements. Assessment of clutter parameters is the subject for an additional line of inquiry for subsequent target recognition algorithms.

4.2   Surface Laid Objects

A short (8") section of 6" diameter schedule 40 pipe is terminated with a 6" diameter steel plate on one end and a concave copper shell that has been pressed into the other end (see Fig. 4.1-left). This target was placed on compacted dry soil with the copper side facing the scanner and oriented such that the cylinder axis and the transceiver axis are collinear at the midpoint of scanner travel. The depression angle was set to 15° and the target was placed 4 m out from the center of the scanner for an initial data collection. The data collection was then repeated with a section of chain link fence placed between the scanner and the target (see Fig. 4.1-right). The duration of the acoustic excitation signal was increased from 10ms to 40ms when the fence section was introduced into the scene to illustrate independence from this parameter. The full field reconstruction domain images for both scenarios are shown in Fig. 4.2. In both reconstructions, the target is clearly distinct from other structures in the scene that contribute acoustic scatter. The 2-dimensional signature plots shown in Fig. 4.4 are produced by spotlighting only the area around the targets of interest. The broadside section of the 2-dimensional signature is calculated by averaging magnitudes across a 5° width of the aspect angle centered at 0° . This so-called one-dimensional signature is often a more readily understood presentation to make a comparison. Figure 4.4 shows that the fence and chirp duration have little impact on the signature. This is in sharp contrast to a SAR image where the fence section would be an opaque barrier and prevent an imaging.

4.2.1   Targets Interactions

Despite spotlighting, ground interaction can have a meaningful influence on SAA signatures. This is because the local ground interactions are not removed by the spotlight aperture. Two case studies are discussed in this section to illustrate this point.

4.2.2   Concave Capped Cylinder on Dry Soil and Grass

The first example compares the signature of the same concave capped cylinder discussed in the previous section with one made in a comparable measurement scenes with tall uneven grass instead of the compacted soil. Fig. 4.5 shows the target from the vantage point of the scanner at mid-travel on both surfaces as well as the reconstructed image.

4.2.3   Proximity to Ground

Multipath reflections between the target and ground are affected by the proximity of the target relative to the ground. This effect is demonstrated using three rigid spheres (bowling balls) placed in a line parallel to the scanner with the chain link fence in the scanner's foreground. One rested on the ground and the other two were elevated by one and two inches respectively. The full field scene (left), an elevated target (center) and the reconstructed image (right) are shown in Fig. 4.7.

The one- and two-dimensional signatures generated from the spotlight section of the reconstructed image are shown in Fig. 4.8. Although the differences seen in these plots are solely attributed to the elevation, extracting the actual evaluation from this data would be require *a priori* knowledge of the target and ground.

4.2.4 Imaging Soft Targets

The targets in the earlier examples were largely simple geometries with hard surfaces and compact structures. More complex targets and scenes are described below in an experimental effort to identify factors that affect the image of a structure. The first example shown in Fig. 4.9, is a supine student centered in the scan range. The acoustic image indicates that it is the higher acoustic impedance regions of the target that result in the highest image amplitudes.

Pair of 3mm
optical fiber
cables   Six nylon cords

Folded aluminum
retro-reflectors

1/8"   3/16"   1/4"   3/8"   1/2"   5/8"
3.2mm 4.8mm 6.4mm 9.5mm 12.9mm 15.9mm

Figure 4.2: (left) A joined pair of optical fibers, (center) six braided nylon cords of increasing diameter (left) folded aluminum retroreflector.
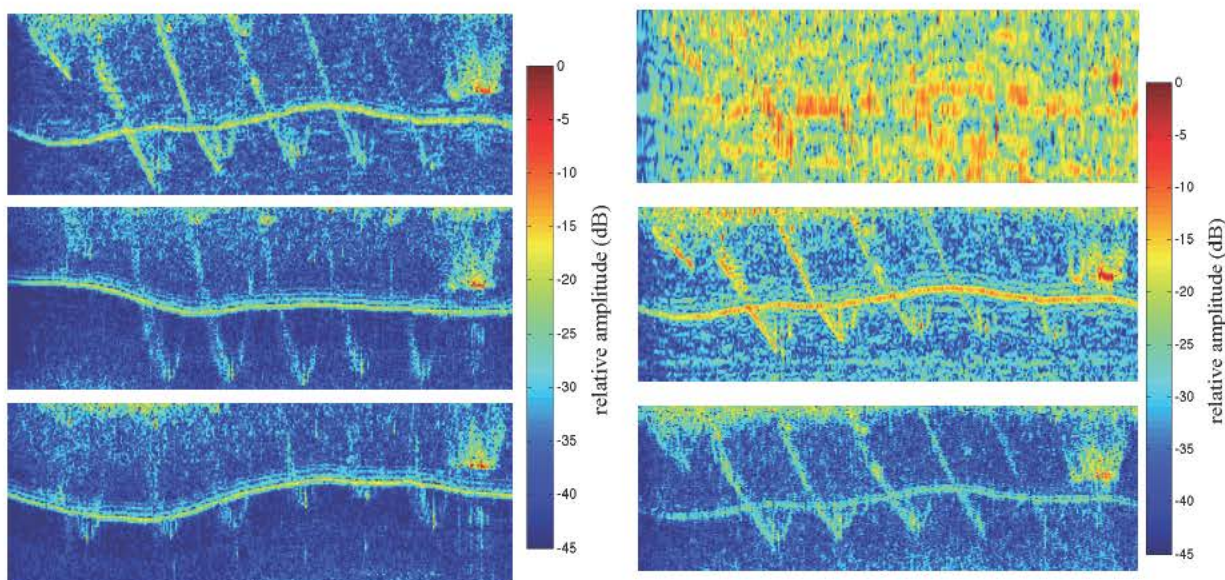

Figure 4.3: (left) Decrease in acoustic return from the nylon cords as the angle relative to the transceiver path increases: 10° (top left), 20° (center left), 30° (bottom left). Cord Diameters increase from right to left: strong return at the right end of each image is a series of metal retroreflectors places as fiducials. (right) Images of cords at 20° relative to the roadway, filtered into octave frequency bands: (top right) 2-4 kHz, (center right) 4-8 kHz, (bottom right) 8-15 kHz.

Figure 4.1: (left) The concave capped cylinder is shown behind the chain link propped so that copper shell is directed toward the scanner. (right) A section of chain link fence in place in the scanner range. Note that the target was not in place for the photo.
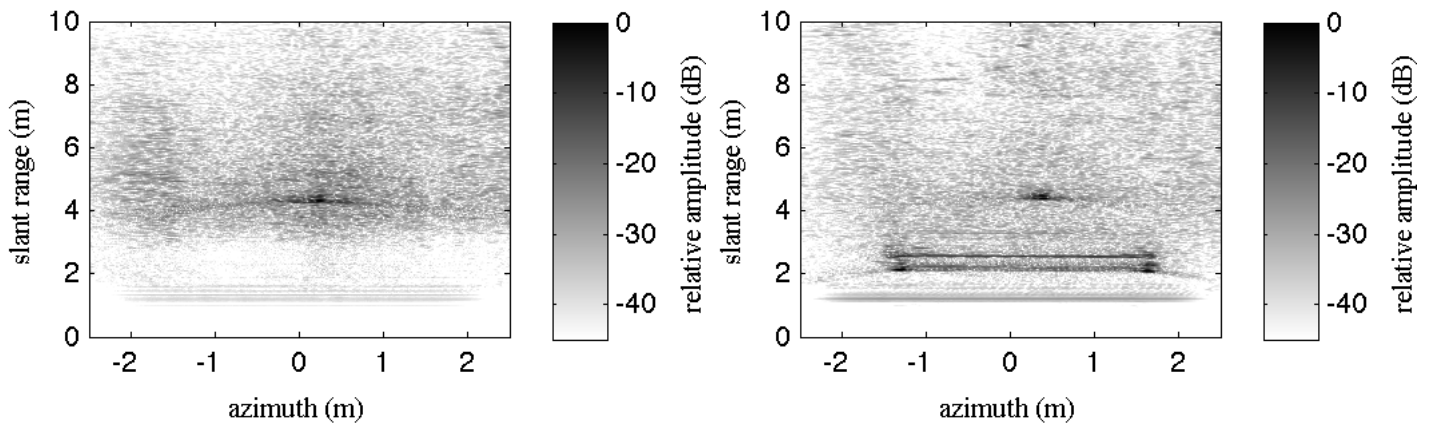

Figure 4.2: The pair of reconstructed SAA images differ as a result of the presence of chain link fence section placed in the scan field between the target and SAA imaging system. The image on the left is the unobstructed measurement. The two parallel lines at a slant range just beyond two meters result from the backscatter from the top and bottom poles that frame the fence section.
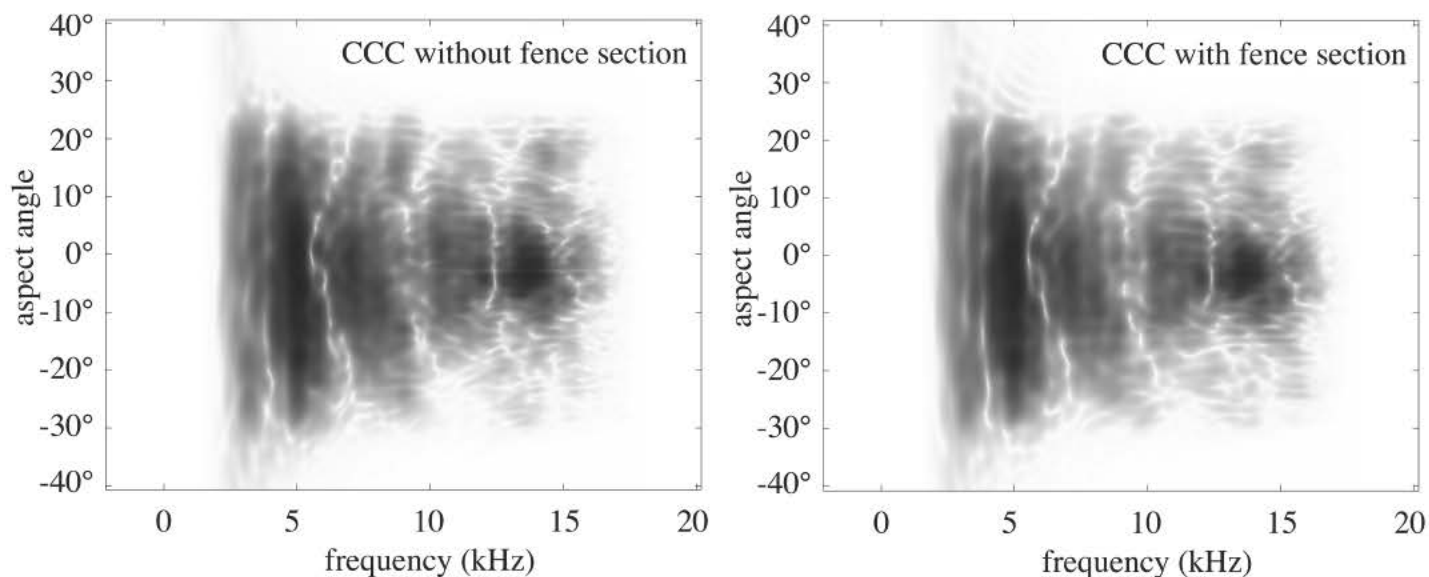
Figure 4.3: The pair of 2-dimensional signature plots appear substantially similar despite the presence of the chain link fence section in the scan field of the signature on the right.
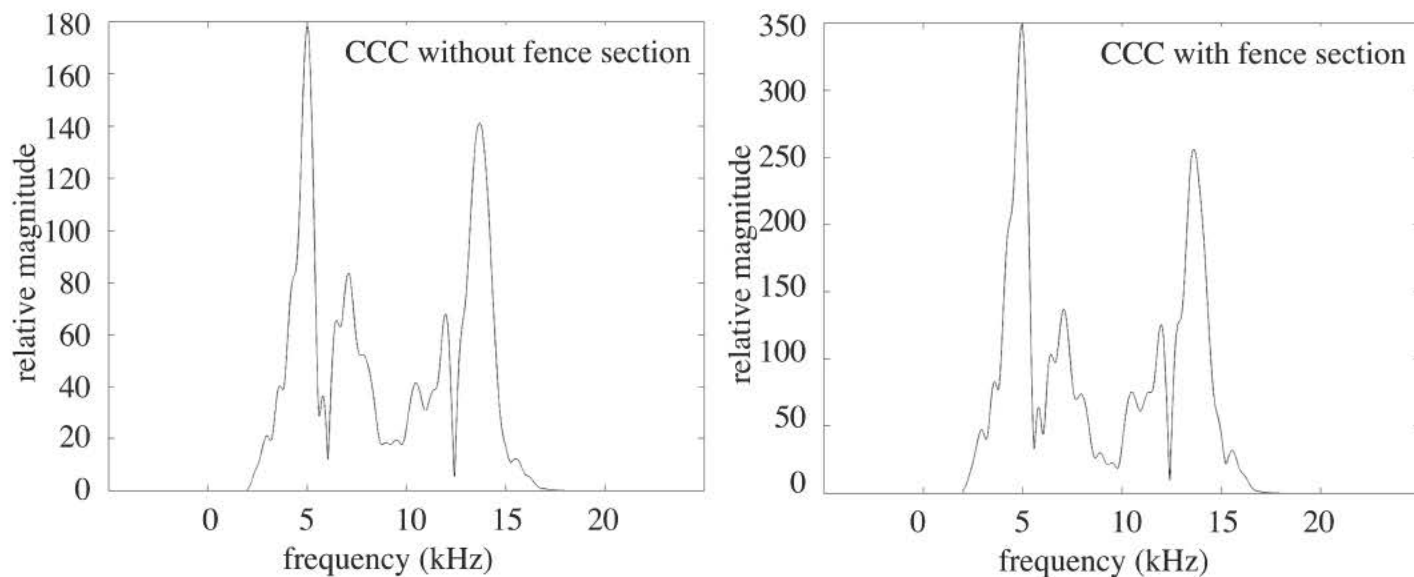

Figure 4.4: A pair of signature magnitude sections produced by averaging over a 5° span of the aspect angle. This pair of plots illustrates that the signatures are independent of the chirp duration.
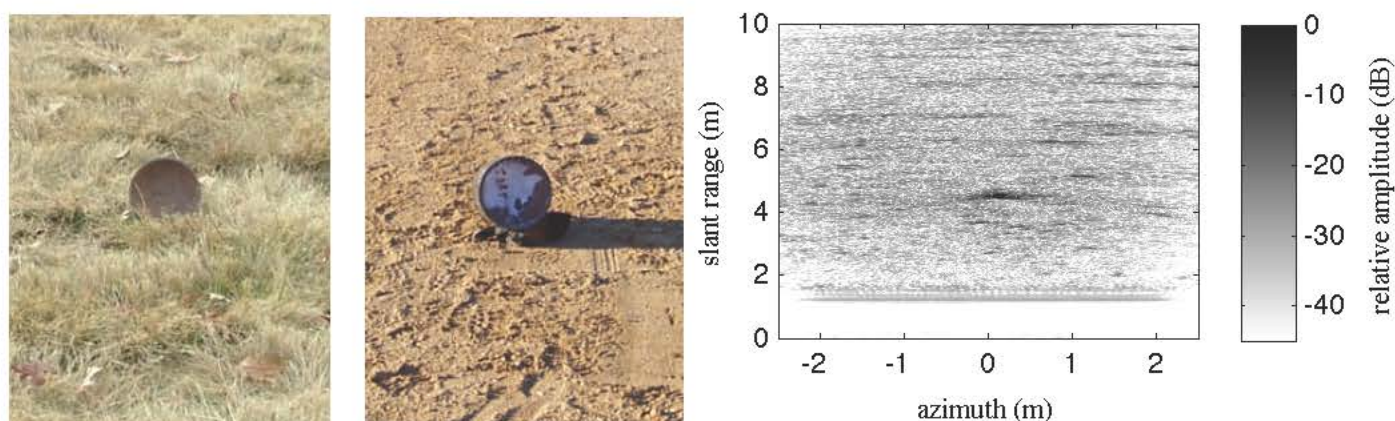
Figure 4.5: The concave capped cylinder is shown placed on dry soil (left) and in uneven grass (center). The image reconstruction (right) shows a few dB increase in target strength over the full field of the measurement but little change in the location of the target of interest.

Figure 4.6: The two-dimensional signature (left) of the CCC placed on grass shows some differences from those shown in Fig **??**. These differences are further revealed in the one-dimensional signature plot shown on the right.

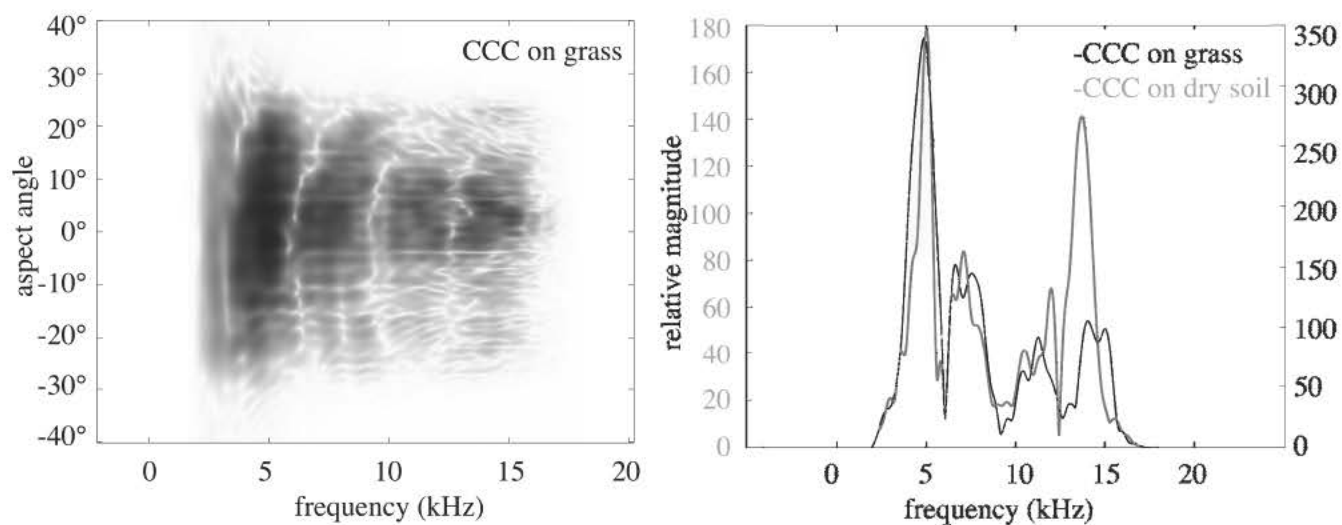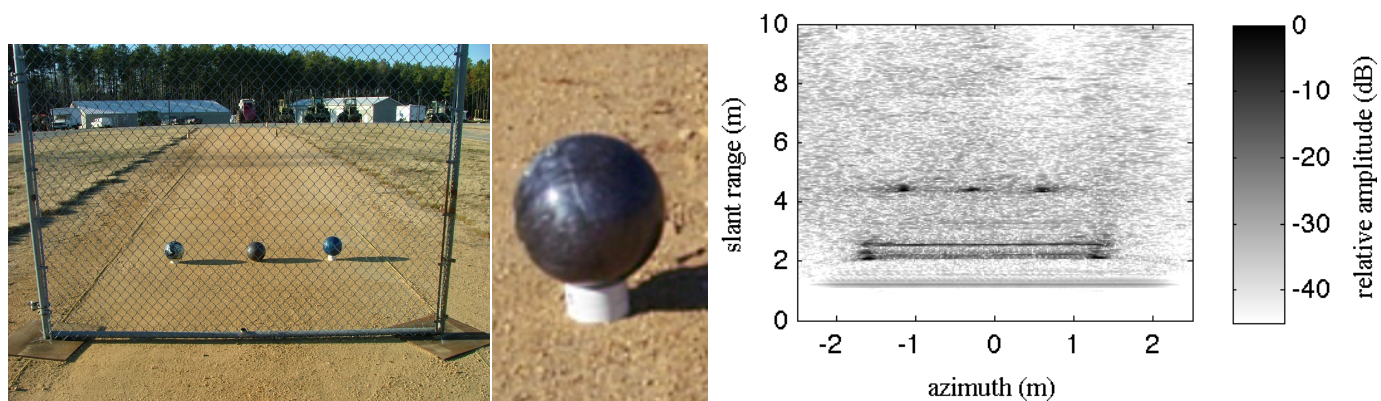Figure 4.7: Three rigid spheres were insonified in a single scan to confirm that target elevation affects signatures. (Left) Full field scene with the targets on the left and right sides elevated by one and two inches respectively. The center sphere is in direct contact with the ground. (Center) Close-up of the sphere that is elevated two inches. (Right) the full field reconstruction image.

Figure 4.8: One and two-dimensional signatures are shown for the three spherical targets depicted in the previous figure.

Figure 4.9: A supine student (left) is imaged (right). The brighter features correspond to her shoes, knees, elbows and chin.

Chapter 5

Acoustic Material Properties in the Outdoor Environment

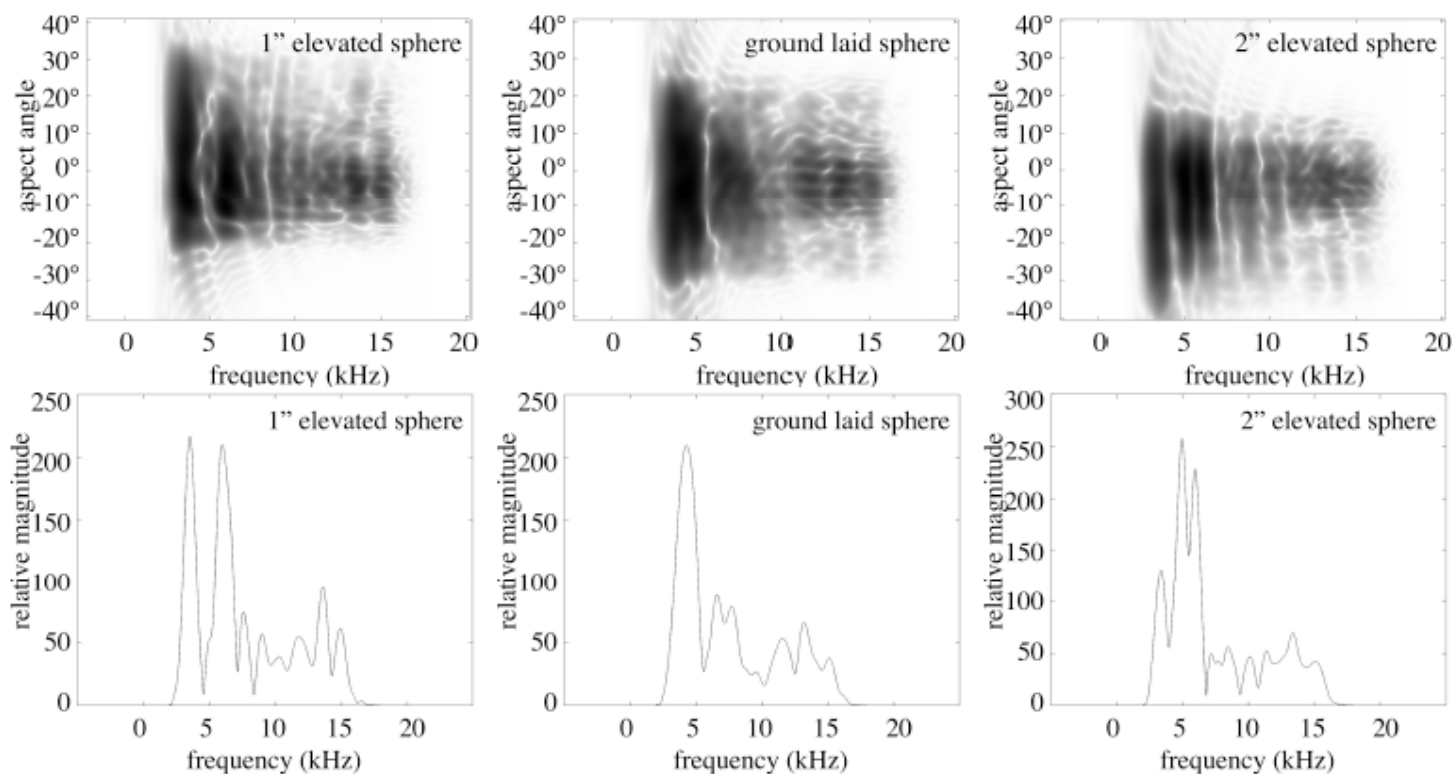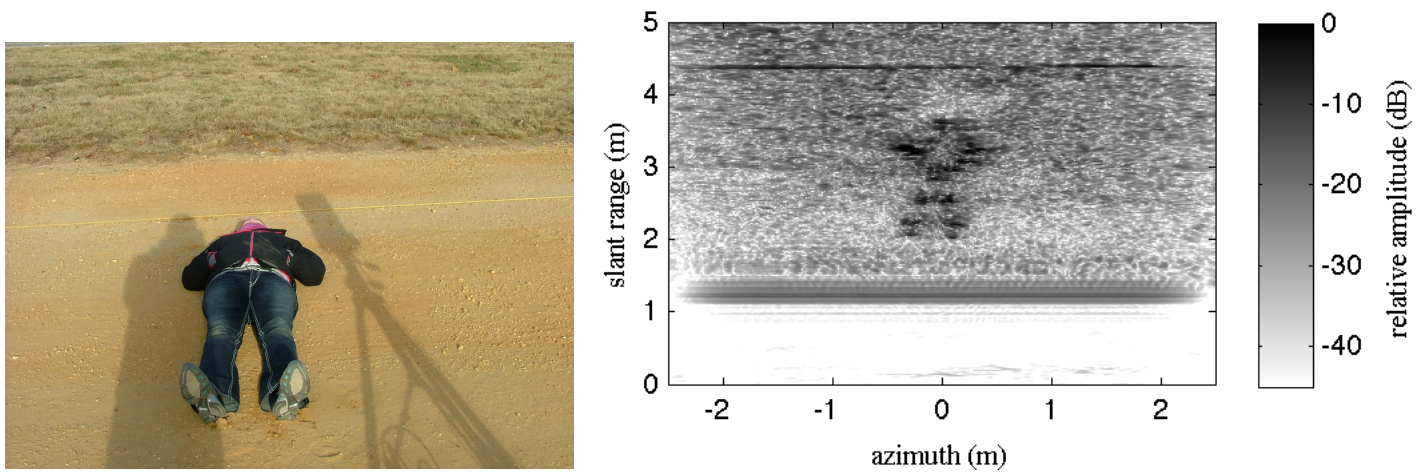CUA designed, fabricated and tested two acoustic impedance tube used to measure acoustic properties of nonconsolidated materials, specifically soils and grass-covered ground. These tubes can be configured vertically for studying acoustic properties of granular materials i.e. soil and dirt. CUA also developed software for data collection and calibration of the impedance tubes.

An equivalent fluid model for describing sound propagation in rigid frame porous media was used to model acoustic behavior of dry and wet soils as well as grass-covered and -uncovered ground. The model requires six parameters, i.e. porosity, tortuosity, flow resistivity, thermal permeability and viscous and thermal characteristic lengths. are measured separately. While flow resistivity was measured, the remaining five parameters were found by fitting procedure (optimization process).

Theoretical models of sound propagation in porous media and acoustic measurements were used to explore the effects of water and vegetation (grass blades and roots) on the sound absorption and reflection of grass-covered ground. The acoustic and flow resistivity measures show that there is minute differences between the acoustic-soil interaction behavior between a root substrate with and without grass. Particularly with the soil samples, moisture encouraged broadband absorption in the higher frequency limits of the acoustic impedance measurements system compared to dried soil.

5.1 Motivation

The CUA research using a side scanning synthetic aperture acoustic imaging device in outdoor settings presented an issue that needed investigation. In these measurements, sound was projected at targets and backscattered sound was recorded. Targets lying in grassy terrain, regardless of sound energy or frequency range, become difficult to detect using the imaging system. This realization motivated research to understand the cause of these effects. This thesis describes an experimental study of samples of isolated soil, grass with root substrate, and sheared root substrate under both wet and evaporated conditions. These measurements were used to characterize sound absorption from grass and soil under various conditions.

Soil itself is a porous medium, consisting of solid matter and voids that can contain air or water. Characterization of porous media has a history dating at least to 1961 with the work of Biot [8]. This

subject of research has continued over the past 50 years [9]; however, specifically characterizing grasses and soil interactions with sound measurements has yet to be thoroughly investigated. Recently, Horoshenko [10] measured the acoustic properties of low growing plants where he primarily focused on measuring the effects of density, surface area, and orientation of the plants' leaves. During this experiment, Horoshenkov removed the roots from the ground and investigated the ground and plant system separately. The present work builds from Horoshenkov by using similar measurement techniques and treating the grass substrate as single system consisting of roots that secure the plant to the ground and draw moisture up to the plant. The complete structure has a consolidating effect on the soil and the presence of the roots reduce the effective porous volume.

Acoustic impedance soil surface has been studied since 1961 [11] and many authors have created different methods and models to characterize outdoor sound propagation on grass-covered ground. The first study on living grass using an impedance tube was conducted by Dickinson and Doak in 1970 [12]. Then a model that accounted for porosity change with depth was proposed in by Donato in 1977 [13]. Most recently Attenborough [14] wrote a review about outdoor ground impedance models and compared predictions of sound absorption to those models with data. He found that a phenomenological model fit data better than widely used simple models like the single parameter approach given by Delany-Bazley [15].

5.2   Approach and Contributions

This component of the project work seeks to understand the reflection and absorption characteristics of soil with foliage and roots and thus their effect on the quality of acoustic images. Indoor experiments are used to characterize representative samples consisting of grass blades, root systems, and soil using an impedance tube. Acoustic data collected on the samples was compared to existing theoretical models. These results provide an understanding of issues related to this complex outdoor imaging technique. This work presents findings from 6 samples under 2 different conditions (moist and dry) showing frequency dependent absorption of sound. In addition, air flow resistance of each sample was measured in order to better estimate the physical parametersrequired for the theoretical models, enabling comparison to the theoretical models. Ultimately this yields parameters that describe the reflection and absorption behavior of the composite. The work consists of a set of measurements, a comparison of the measurements to pre-existing models, and the development of a new parametric model accounting for moisture content.

5.3   Acoustic Properties of Porous Media: Background

Porous media have been a subject of interest because of their ability for noise and reverberation control. Examples of porous media are cements, ceramics, rocks, building insulation, foams and soil. Characterizing the acoustical properties of these materials is challenging due to their complex structures and requires knowledge of several physical attributes. These physical attributes are the material's porosity, permeability, tortuosity, flow resistivity, and both the viscous and thermal characteristic lengths. Most of these are difficult to independently measure. Predictive models have been developed by Biot [8], Delany and Bazley [16], Johnson et al. [17], and Wilson [18] for rigid porous materials. The most effective way to account for dissipation of sound in porous media is to model a medium with an equivalent fluid where the wavenumber and characteristic impedance are expressed as complex quantities.

The simplest equivalent fluid models were proposed by Delany and Bazley [16] and Miki [19]. Their models require only one parameter, i.e. flow resistivity, and were successful for predicting the characteristic impedance and wavenumber of porous media with highly porous materials like fibrous structures. However, these models are were proven to be inaccurate CIT(?umnova) for materials with low porosity like the majority of granular materials.

The most robust and widely used equivalent fluid model were developed in the last decades by Johnson et al. [17], Champoux and Allard[20], and Lafarge[21]. This model, commonly called the JCAL model (from the initials of its authors) uses six physical parameters that can be measured independently by using non-acoustical tests. The six physical parameters consist of porosity, tortuosity, flow resistivity, thermal permeability and viscous and thermal characteristic lengths. Five of these are difficult to physically measure, however, flow resistivity can be measured with the proper measurement system.

5.4 Equivalent Fluid Models

Momentum and mass conservation equations for plane wave propagation in the x-axis in a lossless fluid can be formulated in the frequency domain as follows

$$-i\omega p = -K\frac{\partial u}{\partial x} \tag{5.1}$$

$$-i\omega \rho_o u = -\frac{\partial p}{\partial x} \tag{5.2}$$

In Eqs. 5.1 and 5.2, p is the acoustic pressure, u is the particle velocity, K is the bulk modulus of the fluid ($K = \rho_o c^2$ speed of sound in the fluid), and ρ_o is the density of the fluid. Bulk modulus and density are real constants. In most common free field applications, air is considered as lossless fluid and Eqs. 5.1 and 5.2 can be applied without approximations. However, when acoustic waves travel in narrow channels (much smaller than the acoustic wavelength) viscous and thermal losses occur in proximity of the walls of those channels. For traveling waves in channels, the governing equations will now be written as

$$-i\omega p = -K(\omega)\frac{\partial u}{\partial x} \tag{5.3}$$

$$-i\omega \rho(\omega) u = -\frac{\partial p}{\partial x} \tag{5.4}$$

where density $\rho(\omega)$ and bulk modulus $K(\omega)$ are now frequency dependent complex quantities because of viscous and thermal losses. A rigid frame porous media can be modeled as a network of channels or pores and sound propagating through this medium can be described as

$$-i\omega \phi p = -K(\omega)\frac{\partial u}{\partial x} \tag{5.5}$$

$$-i\omega \rho(\omega) u = -\phi\frac{\partial p}{\partial x} \tag{5.6}$$

where ϕ is the porosity of the medium. Porosity, a real constant, is the ratio between the volume of the pores (filled with air) and the total volume of the porous medium. For this analysis, sound speed, c and wavenumber, Γ in a porous media need to be defined. These complex quantities are given as

$$c = \sqrt{\frac{K(\omega)}{\rho(\omega)}} \tag{5.7}$$

$$\Gamma = \omega\sqrt{\frac{\rho(\omega)}{K(\omega)}} \tag{5.8}$$

5.5 Single Parameter Model

The complex wavenumber, Γ and the characteristic impedance, Z_c for many fibrous materials with porosity close to 1 were measured by Delany and Bazley[?] in 1970 over a wide range of frequencies. They found that the complex wavenumber and characteristic impedance depended mainly on the excitation frequency and the static flow resistivity, σ_o of the material. This static flow resistivity is a measure of the resistance of the material to the flow of air through it.

Delany and Bazley proposed the following empirical expression for Γ and Z_c:

$$Z_c = \rho_o c\sqrt{\frac{\alpha_\infty}{\phi}}\left(1 + 0.0571X^{-0.754} - j0.087X^{-0.732}\right) \tag{5.9}$$

$$\Gamma = \frac{\omega}{c}\sqrt{\alpha_\infty}\left(1 + 0.0978X^{-0.7} - j0.0189X^{-0.595}\right) \tag{5.10}$$

where ρ_o and c are the air density and the speed of sound in air and X is a dimensionless parameter

$$X = \frac{\rho_o\omega}{2\pi\sigma_0} \tag{5.11}$$

For these empirical expressions to be valid, the authors suggested that $0.01 < X < 1$. These boundaries can be seen as frequency limits for a given material. The Delany and Bazley model does not provide a perfect prediction of acoustic behavior of all porous materials in the frequency range previously defined. Nevertheless, these expressions are widely used and can provide reasonable approximations for Γ and Z_c.

A slightly different empirical expressions for Γ and Z_c proposed by Miki are:

$$Z_c = \rho_0 c_0\left(1 + 0.0571X^{-0.754} - j0.087X^{-0.732}\right) \tag{5.12}$$

$$\Gamma = \frac{\omega}{c_0}\left(1 + 0.109X^{-0.618} - j0.160X^{-0.618}\right) \tag{5.13}$$

This model also applies in the frequency range $0.01 < X < 1$.

Horshenkov *et al.*[10] showed recently that this model is able to provide satisfactory predictions of the fundamental acoustic properties of foliage and soils. However, in addition to the flow resistivity data, the model used by this group relies on the data which was measured directly and linked to the morphology of a specific plant.

5.6   JCAL Model

Acoustic behavior of rigid frame porous materials can also be described by the JCAL model[17]. In this model complex density and bulk modulus are functions of angular frequency and six physical parameters. Their expressions are as follows:

$$\rho(\omega) = \rho_0 \left(\alpha_\infty + \frac{\sigma_0 \phi}{-i\omega\rho_0} \sqrt{1 - i\omega \frac{\eta}{\rho_0} \left(\frac{2\rho_0\alpha_\infty}{\sigma\phi\Lambda} \right)^2} \right) \tag{5.14}$$

$$K(\omega) = \rho_0 c_0^2 \left(\frac{\gamma - 1}{1 + \frac{\eta\phi}{-i\omega\rho_0 N_{Pr} k_0'} \sqrt{1 - \frac{i\omega\rho_0 N_{Pr}}{\eta} \left(\frac{2k_0'}{\phi\Lambda'} \right)}} \right)^{-1} \tag{5.15}$$

where α_∞ is tortuosity, ϕ is porosity, Λ is viscous characteristic length, σ_0 is static flow resistivity, η dynamic viscosity of air, Λ' is thermal characteristic length, k_0 is thermal permeability, N_{Pr} is Prandtl number. Tortuosity values larger than 1 indicate that sound waves have to travel through a tortuous path while crossing the medium. Viscous loss increases with greater tortuosity. Characteristic viscous length is equivalent to the hydraulic radius but for more general microgeometries. The static flow resistivity is proportional to the inverse of viscous permeability $k_0 = \frac{\eta}{\sigma_0}$. Characteristic thermal length and thermal permeability are thermal equivalents to the characteristic viscous length and permeability. Characteristic impedance Z_c and complex wavenumber Γ can therefore be evaluated:

$$Z_c = \frac{1}{\phi} \sqrt{\rho(\omega)p(\omega)} \tag{5.16}$$

$$\Gamma = \omega \sqrt{\frac{\rho(\omega)}{K(\omega)}} \tag{5.17}$$

The main advantage of this model is that it works for any frequency range and porosity value.

Ground surfaces of low porosity may be considered acoustically hard according to Attenborough [22] [14], and vegetation covered ground is to be considered acoustically soft. In general, porous ground surfaces are elastic as well as porous and their elastic response may be significant at high amplitude and low frequency noise. But, for more typical noise predictions such as for noise from surface transport, the choice of impedance models can be confined to those representing the acoustical properties of airfilled porous materials with rigid frames [14]. Under these circumstances the JCAL model can predict and describe the acoustic behavior of grass covered ground with good approximation. However, determination of six parameters is needed. For the purpose of exploring the acoustic effects of the water, grass blades and roots on reflection and absorption coefficient of grass covered ground, comparisons between multiple experiments performed on dry and wet soil and grass covered and uncovered ground can be used. Then optimization procedures can be used to fit the JCAL model to the data and estimate the unknown parameters of the model. The determination of those parameters will be used for interpreting the data.

5.7 Impedance Tube

Impedance tubes are a traditional tool in acoustics labs that that a history that dates back to the 1970s. Most acoustics texts have some discussion. These include Kinsler and Frey[23], Pierce[24], pp. 111-113, Blackstock[25],pp 142-143. There are a number of national and International measurements standards including American Society for Testing and Materials (ASTM E 1050-98), [citation needed].

In the CUA Acoustics lab we have built two impedance tubes. The larger tube has an inner diameter of 3.5" (88.9mm) is for low frequency experiments (200-2200Hz) and the smaller tube has a 1" inner diameter (25.4mm) which operate over a 700-8000Hz frequency band. See Fig. xx. These tubes were designed to be flexible and modular so that they can be used with a wide variety of target samples.

This chapter describes the theory and design of the two CUA impedance tubes. Then there are section on the use of the tubes, and software for acquisition and data processing.

5.7.1 Impedance Tube Principles

The complex acoustic pressure measured at each microphone position is the superposition of the incident and reflected waves as seen in Fig. 5.1. If we assume that only plane waves can propagate in the tube
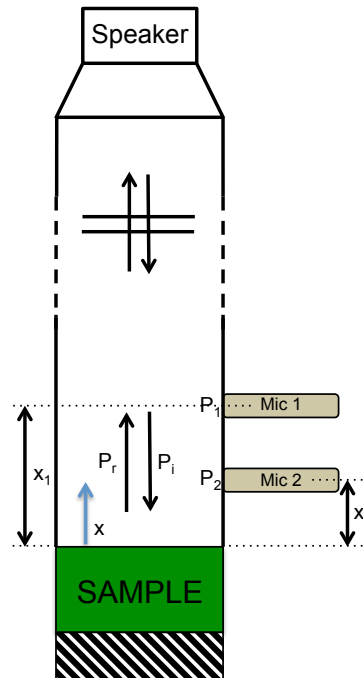

Figure 5.1: The impedance tube, here show in a vertical orientation has a speaker hosed at the top, two microphones flush mounted the the inner wall of the tube, and a test sample that is rigid mounted to lower end of the tube. The speaker launches sound toward the test sample which is measured by the two microphones.

because the excitation signal is restricted to frequencies below the cutoff frequency the sound field at some

position x_1 in the tube can be expressed as

$$p(x_1, t) = P_i e^{i(\omega t + kx_1)} + P_r e^{i(\omega t - kx_1)} \tag{5.18}$$

If we assume that the reflected wave amplitede, P_r is related to the incident pressure amplitude, P_i by

$$P_r = R(\omega)P_i \tag{5.19}$$

were $R(\omega)$, referred to as the reflection coefficient is a complex function of frequency. The reflection coefficient is one of the key results of any impedance tube measurements. The acoustic pressure at the location of the second microphone, x_2 us a similar expression. A transfer function, H_{12}, of these two microphone signals can be formed as.

$$H_{12} = \frac{P_2(\omega)}{P_1(\omega)} = \frac{P_i e^{jkx_2} + R(\omega)P_i e^{-jkx_2}}{P_i e^{jkx_1} + R(\omega)P_i e^{-jkx_1}} \tag{5.20}$$

Note that the time dependence in each of the plane wave expression can be factored and canceled when the transfer function is formed.

In Eq. 5.20, P_1 and P_2 are the acoustic pressures measured at each respective microphone, P_i is the incident pressure, k_0 is wave number in air, ω is angular frequency, x_1 and x_2 are the distances between the sample surface and microphone. The reflection and absorption coefficients, $R(\omega)$ and α respectively of the sample are calculated using the transfer function with Eqs. 5.21 and 5.22 respectively [26] [27].

$$R(\omega) = \frac{e^{jk_0^{x_1-x_2}} - H_{12}}{H_{12} - e^{jk_0^{x_1-x_2}}} e^{2jk_0x_1} \tag{5.21}$$

This calculation gave us the reflection coefficient, Allard gives an expression for the absorption coefficient as:

$$\alpha(\omega) = 1 - R(\omega)^2 \tag{5.22}$$

In addition, Allard gives an expression for surface Impedance, $Z_s(\omega)$

$$Z_s(\omega) = \rho c \frac{1 + R(\omega)}{1 - R(\omega)} \tag{5.23}$$

where ρ is the density of air, and c is the sound speed of air.

5.7.2 Validation of the Impedance Tube Measurements

Blue aquamarine sand with grain diameters ranging from 500-600 μm was used to confirm accurate measurement of the system. Packed spherical particles have acoustic properties that demonstrate the effect of interstitial space within the material; interstitial spacing allows for the sound to become trapped between the spheres. The cell model was used for estimating the acoustic parameters of sand [28] [29]. This theoretical model can estimate σ, k_0', Λ, Λ' and α_∞ of spherical particles as long as the radius r and porosity are known. A sample containing 5 cm of loosely packed blue aquamarine sand had $r = 250$ μm and porosity

r (μm)	ϕ	α_∞	σ (kPa s/m^2)	Λ (μm)	k_0' (nm^2)	Λ' (μm)
250	0.41	1.72	65.8	79.9	69.2	115.8

Table 5.1: Sand parameters estimated using cell model

$\phi = 0.41$. Based on the cell model the parameters shown in Table 5.1 were estimated.

The parameters were then used in the Johnson-Champoux-Allard-Lafarge (JCAL) model[17] expressed as Eqs. 5.14 and 5.15. An acoustic impedance tube measurement of the blue aquamarine sand was performed to determine reflection and absorption coefficients. Characteristic impedance and wavenumber were evaluated using Eqs. 5.16 and 5.17. The JCAL model fit with the data Fig. 5.2 showing that the system provides reliables measurements.

5.7.3   Calibration of an Impedance Tube

The impedance tube needs to be calibrated before any set of measurements in order to account for microphone phase mismatch. To perform the calibration of the tube an absorbing material with known acoustic properties is used. A sample of Melamine foam, 5 cm thick was used to perform the calibration. The goal of the calibration measures is the estimation of a correction factor. All the transfer functions measured using the samples of interest will be multiplied by this factor to account for the phase mismatch between the microphones.

The impedance tube measurement system was calibrated using materials with known acoustic properties in order to confirm accurate measurement of the system. Melamine foam 5 cm (1.97 in.) in thickness was used to perform this calibration measurement. The calibration measures the correction factor which accounts for phase mismatch between the microphones.

5.7.4   Soil Experiments

The samples were encased in a 4 ft (122 cm) by 3 ft (91.4 cm) wooden box, as shown in Fig. 5.3. The Miracle-Grow fertilized soil was initially sieved with a ASTM E11 sieve to remove all rocks, bark, other organic matter. The sieve also ensured a grain size less than 4.75 mm in diameter. The soil is initially approximately 4 in (10.12cm) in depth when laid in the soil plot. Kentucky perennial grass seeds are spread over the half of the soil with approximately 40 seeds planted per square inch (6.45 m^2). Over the course of 3 weeks the grass is grown until the height of each blade is 4 to 5 inches (10-13 cm).

The grass was kept indoors and keep at the indoor temperature of 72 degrees. It was grown from a seedling completely indoors while receiving exactly 6 hours of artificial sunlight from hydroponic grow lights. Each side of the sample plot was watered daily 1.25 L of tap water evenly spread using a watering can.

Prior to impedance tube measurement the samples were cut using a plunger cutter with a 3.5 in (88.9 cm) diameter. This ensures all the layers evenly fit the tube without air gaps between the substrate and the sample holder walls (vital to accurate impedance measurement). The samples were first placed in the flow resistivity rig where flow rate and pressure measurements were taken. The flow resistivity parameter was extrapolated from these measurements. The sample holder was then attached by cam latched to the

impedance tube. The weight of the moist samples within their respective holder was taken.

After the initial impedance tube measurements, the samples were dried, and the initial moisture content was estimated in accordance with ASTM C70-13 using the burn-off method. The impedance tube sample holders were placed into a oven set to 110° C and cooked for 24 hours removing nearly all the moisture within the sample. The desiccated samples were weighed and the moisture content was computed based on the weight difference. The desiccated samples were measured with the impedance tube for the second time, as dry specimens.

5.8   Measurement Parameters

5.9   Post processing of the data and fitting procedure

Data fitting was achieved using a built-in Matlab function "fminsearch". In this function a Nelder–Mead simplex direct search algorithm is implemented. In this study,"fminsearch" has been used to find a set of parameters that minimize the difference between a chosen model and the measured reflection coefficient at all frequencies. First the "Cell model" which uses of only two parameters, pore radius and porosity, was employed to fit the data. This simple model allows initializing the search of a multiple-variable model like the JCA model. The porosity and flow resistivity used for the JCA model were then used to initialize the parameter search of the Delany-Bazley and Miki models. Predicted parameters values of these models are tabled in table 5.3.

5.10   Flow Resistivity and Extracted Parameters

For each moist sample, the flow resistivity was physically measured in a flow resistivity measurement system. The results are displayed in Figs. 5.1 and 5.2. The samples then underwent acoustic measurements in an impedance tube. These measurements uncover the sample characteristics. The combination of these acoustic characteristics and pre-existing theoretical models allows for estimation of other sample parameters. These extracted parameters provide further insight into the sample in its different states and its potential behavior with respect to sound propagation. Static flow resistivity is one of those parameters, which was both measured and estimated by model fitting for this experiment. Measured and estimated values of flow resistivity of grass samples reveal that the grass blades do not contribute to the flow resistivity of the sample. In Fig. 5.1 the flow resistivity is slightly lower than that of its root-substrate (without blades).

It is important to consider the way the sample thickness is evaluated. For example the sample thickness significantly influences the flow resistivity value. If the root-substrate and the blade height are combined, increasing the overall sample thickness there will be an underestimation of the flow resistivity. Both the physical measurements and the models reflect this result when the blades are considered a part of the sample thickness. It is possible to explain this phenomenon by the fact that between the cutting process and the replacement of the sample into the flow resistivity rig the pores structure might have been slightly modified. These results lead to the conclusion that the grass layer did not contribute to a significant increase of the flow resistivity and that their presence does not affect the absorption property of the soil.

5.11   Moisture Effects in Soils

Wet samples were thicker than their dry counterpart. This cannot be simply justified by the absence of water in the dry sample. The amount of water in the sample, measured by weight difference, can only justify 27.6% reduction in volume or 1.1 cm in thickness of the dry sample. The remaining thickness reduction must be dude to the collapse of the pore structure that occurred after the desiccation of the sample. The effects of these phenomena are observed through the parameters value predicted by the fitting of Delany-Bazley, Miki and JCA models to the absorption coefficient of the sample. In particular, only JCA and Delany-Bazley models predict a flow resistivity values that are in agreement with published data**??** ($\frac{kPa \ s}{m^2}$) and both show that flow resistivity decreases from wet to dry. However, the data fit shows that only JCA capture the acoustic behavior of both wet and dry samples. The JCA model reveals also that a wet sample has lower porosity compared to its dry equivalent, which is expected since the water fills the pores, and that tortuousity. Thus reduction of flow resistivity and increase of porosity suggest that the pores in dry soil samples are narrower and numerous. With the Johnson-Champoux-Allard model one can fit the averaged data curve and base the parameters values on the fitting. This model has been shown to be the most robust phe- nomenological model for sound absorption of rigid-frame porous media. It uses 6 independent parameters: Porosity, tortuosity, flow resistivity, thermal permeability, viscous and thermal characteristic lengths. There is better overall agreement between fitting curve and dry soil data compared to the wet soil data. This model is designed for porous filled with single phase fluid while in the case of soil the pores are filled with both air and water. In the "wet-data" some extra absorption is observed around 400-600 Hz which is not captured by the model as well as at frequency between 1700-2000 Hz "Dry-data" are well fitted by the model except for an extra absorption observed at around 200-300 Hz. We are not entirely sure about this, but the vibration of the superficial layer of the soil might be the cause of it.   JCA model fit in fig. 5.2 shows that wet soil with roots has lower flow resistivity (33.6 $\frac{kPa \ s}{m^2}$) and lower porosity (0.38) than its dry counterpart ($37\frac{kPa \ s}{m^2}$, 0.72 respectively). This was expected since the pores of the wet sample are partially filled with water reducing the porosity of the sample.
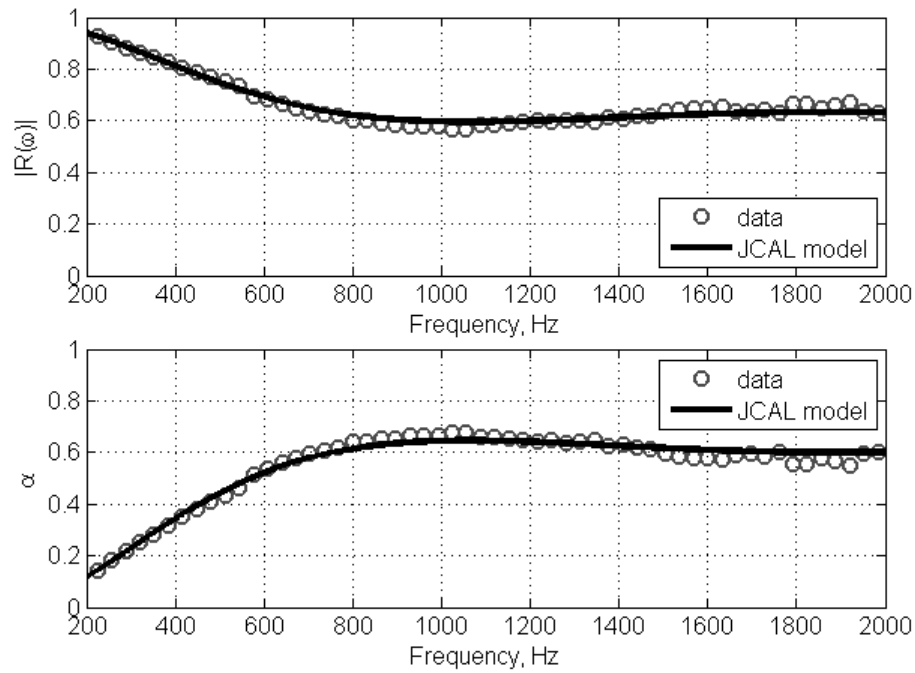
Figure 5.2: (Top) Reflection and (Bottom) Absorption coefficient of blue sand. Sample thickness is equal to 5cm, $\phi = 0.41$, particle radius $r = 250\ \mu m$. Gray circles are impedance tube data. Black line is the JCAL model with parameters estimated using the cell model

Figure 5.3: The sample grow box is show. On the right side is germinated Kentucky perennial grass. On the left side soil that has been sieved to 4.75 mm grain size. The 4 inch grid system marks each sample to be cut

Table 5.2: Excitation Parameters

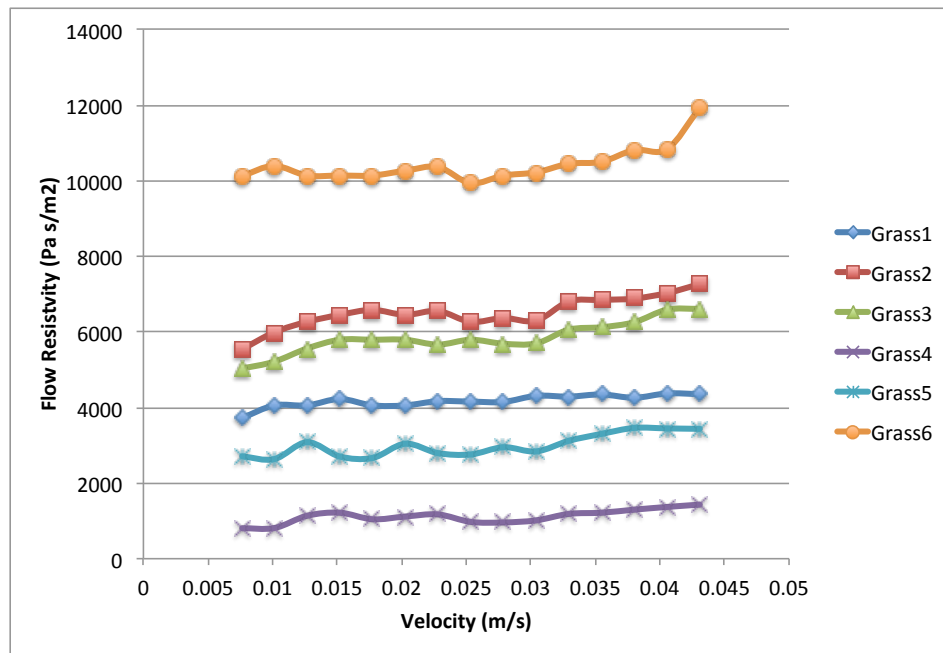| Excitation Parameters	
Chirp Band	100-200 Hz
Chirp Duration	250 ms
Sampling Frequency	40 KHz
Microphone	$\frac{1}{4}$ in. B & K Model 4165 Mic
Sensitivity	50 mV/Pa

Figure 5.1: The flow resistivity measurements of all the grass samples. The flow resistivity is based on the slope of the flow resistivity as it varies with velocity.
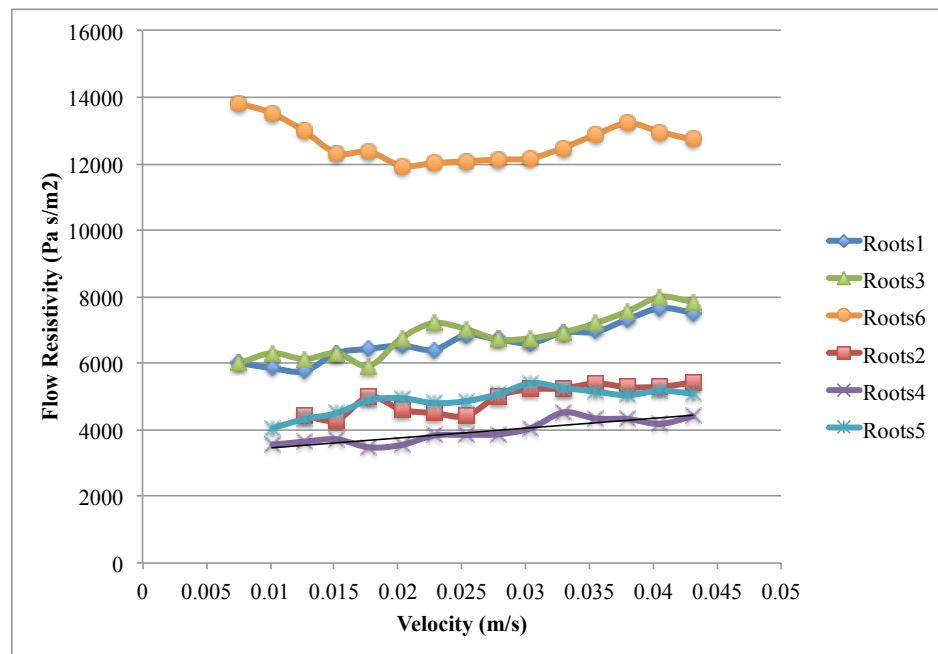
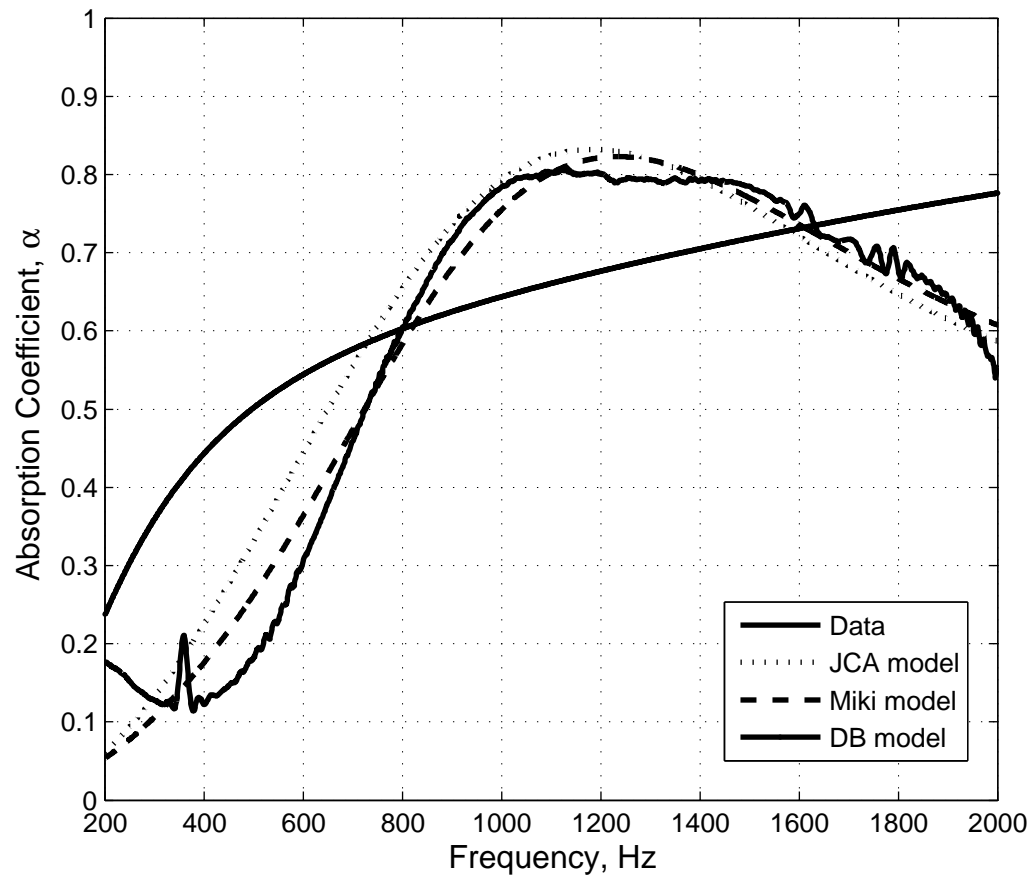Figure 5.2: The flow resistivity measurements of all the root samples.

Figure 5.1: The grass sample that weighed 145.6g, root-ground substrate was 4.4 cm thick and had a moisture content of 36.1%. The grass sample is fitted to the JCA, Delany-Bazley, and Miki models.
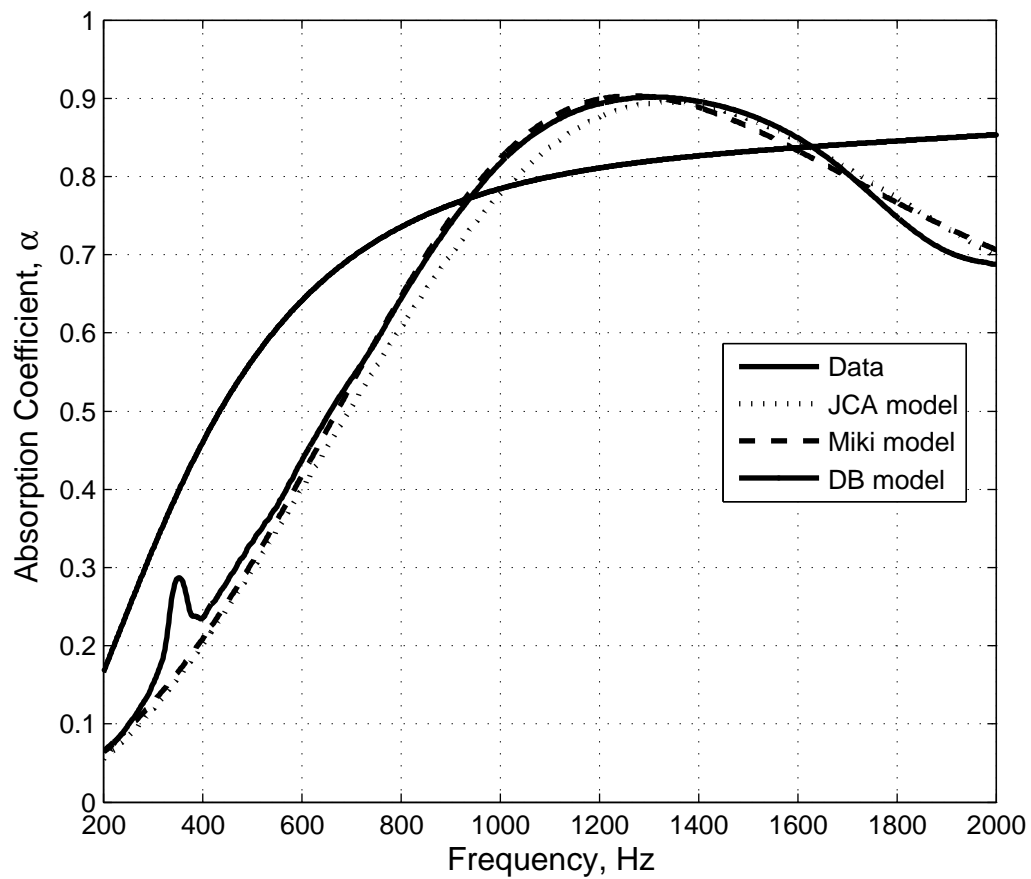
Figure 5.2: The root samples weighed 145.6g, root-ground substrate was 4.4 cm thick and had a moisture content of 36.1%. The moist root sample is fitted to the JCA, Delany-Bazley, and Miki models
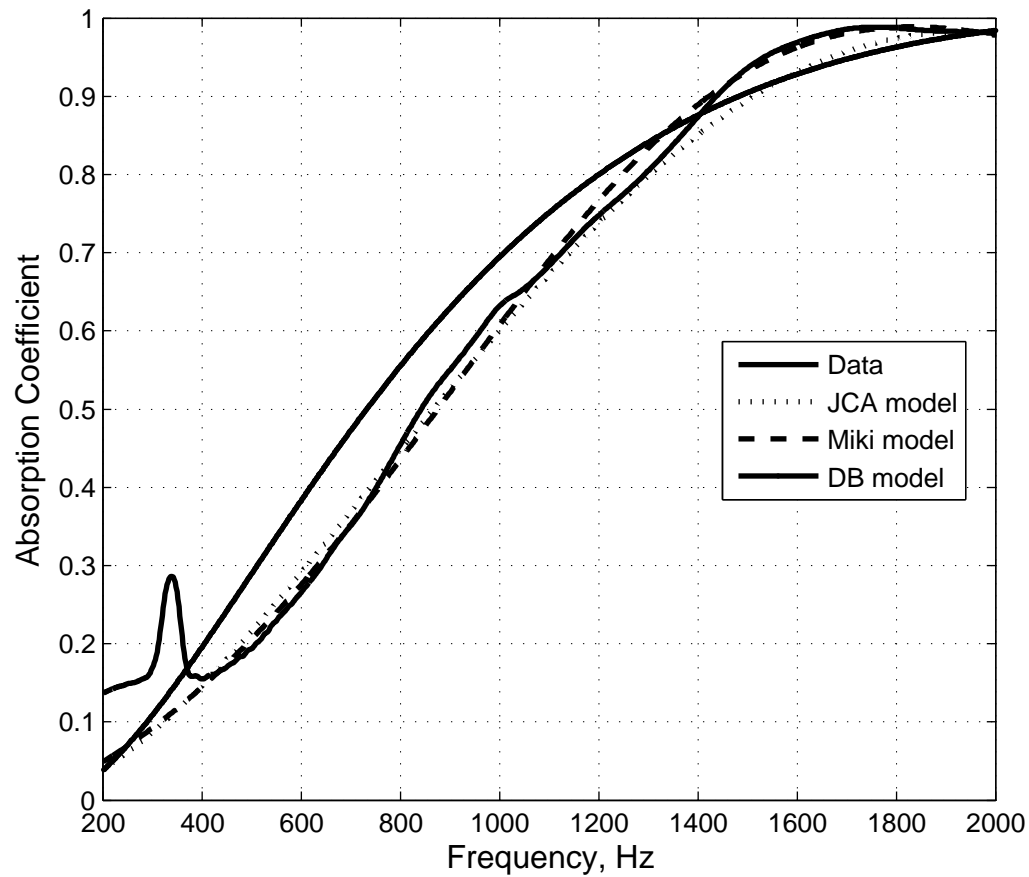
Figure 5.3: The soil sample weighed 86.8 g after dissication. The sample was 2.9 cm thick. The moist and dry soil samples' acoustic impedance data were fitted to the JCA model

Method	Parameters	Wet soil	Dry soil	Covered Grass soil	Wet soil with roots	Dry soil with roots
Direct	Thickness (cm)	4.1	3.3	2.5 + 4.4	4.4	2.9
	Water content (g)	70	0	50	50	0
	Water content (volume %)	27.6	0	5.5	5.5	0
	Eq. water thickness (cm)	1.1	0	0.8	0.8	0
	Flow resistivity	-	-	32.620	36.324	-
Cell model	Eq. radius (mm)	0.314	0.199	0.348772	0.397	8.12E−05
	Porosity	0.44	0.56	0.40	0.38	0.72
JCA model	Porosity	0.44	0.56	0.40	0.38	0.72
	Tortuosity	1.63	1.39	1.74	1.80	1.19
	Flow resistivity	30.797	25.376	36.313	33.641	36.989
	Thermal permeability (m^2)	1.42E−09	1.53E−09	1.26E−09	1.39E−09	9.14E−10
	Viscous characteristic length (mm)	0.112	0.112	0.10863	0.116	8.95E−05
	Thermal characteristic length (mm)	0.166	0.171	0.156807	0.165	0.139
DB model	Flow resistivity (kPa·s/m^2)	54.128	18.501	83.650	88.727	21.968
Miki model	Porosity	0.52	0.65	0.38	0.37	0.59
	Tortuosity	1.66	1.42	1.49	1.59	1.95
	Flow resistivity (kPa·s/m^2)	10.590	11.663	10.792	9.147	12.758

Table 5.3: Physical and Extracted Parameters of Each Sample

Chapter 6

Conclusions

Synthetic aperture acoustic imaging provides a method of rendering outdoor scenes and in the presence of intervening metallic chain link fencing and clutter, i.e., grass. The spotlighting used in the SAA imaging process offers a mechanism for separating various targets in the imaging scene based on the SAA system resolution. The SAA images of targets of interest within a scene appear as local bright spots and are not ideally suited for target identification. This implies that there are limited distinct features in their SAA images for conventional pattern-based automatic target recognition (ATR). In other words, the imaging domain that is used for the visualization of the scene is not the ideal domain for identifying and classifying target since there are usually no distinct geometric features in the images of the targets of interest.

Data shown in this report was collected in a broad range of scenes under different environmental conditions. The aperture for these measurements ranged from a few meter to over 100 meters. For this technique, the measurement range scales with this aperture length and source level. This implies that targets at much grater ranges could be imaged. Ultimately factors including atmospheric turbulence, soil conditions and ambient noise would limit this range. These issues should be the subject for further study.

As a general point, SAA images map spatial acoustic impedance variations rather than changes in dielectric properties. This implies that SAA data can be processed using the same types of tools commonly used in SAR, but that targets like nylon cord, which would not have a strong radar scattering cross-section, are easily identified acoustically. Conversely, structures that would be electromagnetically opaque, like the chain link fence, are transparent acoustically. An important next step in this research is to collect target data using both SAR and SAA to evaluate the benefits of fused data for target classification and recognition.

Bibliography

[1] M. Soumekh. Airborne synthetic aperture acoustic imaging. *Image Processing, IEEE Transactions on*, 6:1545–1554, 1997. 11.

[2] Catherine H. Frazier, Nail ÃĞadallÄś, David C. Munson Jr, and William D. OâĂŹBrien Jr. Acoustic imaging of objects buried in soil. *The Journal of the Acoustical Society of America*, 108(1):147–156, 2000.

[3] Walter Carrara, Ron Goodman, and Ronald Majewski. *Spotlight synthetic aperture radar- Signal processing algorithms*. 1995.

[4] Chris Oliver and Shaun Quegan. *Understanding synthetic aperture radar images*. SciTech Publishing, 2004.

[5] PT Gough and DW Hawkins. *A short history of synthetic aperture sonar*. IEEE, 1998.

[6] Mehrdad Soumekh. *Synthetic Aperture Radar Signal Procession*. Wiley-Interscience, 1999.

[7] M. Soumekh. Reconnaissance with ultra wideband UHF synthetic aperture radar. *IEEE Signal Processing*, 12:21 – 40, 1995. 4.

[8] M. A. Biot. Mechanics of deformation and acoustic propagation in porous media. *Journal of Applied Physics*, 33(4):1482–1498, April 1962.

[9] N. Dai, A. Vafidis, and E. R. Kanasewich. Wave propagation in heterogeneous, porous media: A velocityâĂŘstress, finiteâĂŘdifference method. *GEOPHYSICS*, 60(2):327–340, March 1995.

[10] Kirill V. Horoshenkov, Amir Khan, and Hadj Benkreira. Acoustic properties of low growing plants. *The Journal of the Acoustical Society of America*, 133(5):2554–2565, 2013.

[11] Jq Geertsma and D. C. Smit. Some aspects of elastic wave propagation in fluid-saturated porous solids. *Geophysics*, 26(2):169–181, 1961.

[12] P. J. Dickinson and P. E. Doak. Measurements of the normal acoustic impedance of ground surfaces. *Journal of Sound and Vibration*, 13(3):309–322, November 1970.

[13] R. J. Donato. Impedance models for grassâĂŘcovered ground. *The Journal of the Acoustical Society of America*, 61(6):1449–1452, June 1977.

[14] Keith Attenborough, Imran Bashir, and Shahram Taherzadeh. Excess attenuation and effective impedance associated with rough hard ground. *The Journal of the Acoustical Society of America*, 132(3):1903–1903, September 2012.

[15] Bryan H. Song and J. Stuart Bolton. A transfer-matrix approach for estimating the characteristic impedance and wave numbers of limp and rigid porous materials. *The Journal of the Acoustical Society of America*, 107(3):1131–1152, 2000.

[16] M. E. Delany and E. N. Bazley. Acoustical characteristics of fibrous absorbent material. *The Journal of the Acoustical Society of America*, 48(2A):434–434, August 2005.

[17] David Linton Johnson, Joel Koplik, and Roger Dashen. Theory of dynamic permeability and tortuosity in fluid-saturated porous media. *Journal of Fluid Mechanics*, 176:379–402, 1987.

[18] D. K. Wilson. Simple, relaxational models for the acoustical properties of porous media. *Applied Acoustics*, (3):171–188, 1997.

[19] Yasushi Miki. Acoustical properties of porous materials-modifications of delany-bazley models. *J. Acoust. Soc. Jpn.(E)*, 11(1):19–24, 1990.

[20] Yvan Champoux, Michael R. Stinson, and Gilles A. Daigle. Air-based system for the measurement of porosity. *The Journal of the Acoustical Society of America*, 89(2):910–916, 1991.

[21] Denis Lafarge, Pavel Lemarinier, Jean F. Allard, and Viggo Tarnow. Dynamic compressibility of air in porous structures at audible frequencies. *The Journal of the Acoustical Society of America*, 102(4):1995–2006, October 1997.

[22] Acoustics - determination of sound absorption coefficient and impedance in impedance tubes - part 2: Transfer function method.

[23] L. E. Kinsler, A. R. Frey, A. B. Coppens, and J. V. Sanders. *Fundamentals of Acoustics*, volume New York. John Wiley & Sons, forth edition, 2000.

[24] Allan D Pierce. *Acoustics: an introduction to its physical principles and applications*. McGraw-Hill New York, 1981.

[25] David Blackstock. *Fundamentals of Physical Acoustics*. Wiley-Interscience, 2000.

[26] J. Y. Chung and D. A. Blaser. Transfer function method of measuring inâĂŘduct acoustic properties. II. experiment. *The Journal of the Acoustical Society of America*, 68(3):914–921, September 1980.

[27] J. Y. Chung and D. A. Blaser. Transfer function method of measuring inâĂŘduct acoustic properties. i. theory. *The Journal of the Acoustical Society of America*, 68(3):907–913, September 1980.

[28] Keith Attenborough Olga Umnova. A cell model for the acoustic properties of packings of spheres. *Acta Acustica united with Acustica*, 87(2):226–235, 2001.

[29] Olga Umnova, Keith Attenborough, and Kai Ming Li. Cell model calculations of dynamic drag parameters in packings of spheres. *The Journal of the Acoustical Society of America*, 107(6):3113–3119, June 2000.